The Canadian Mineralogist
Vol. 42, pp. 1283-1314 (2004)

RAMAN SPECTRA OF FLUID AND CRYSTAL MIXTURES IN THE SYSTEMS H_2O, H_2O–NaCl AND H_2O–$MgCl_2$ AT LOW TEMPERATURES: APPLICATIONS TO FLUID-INCLUSION RESEARCH

RONALD J. BAKKER§

Mineralogy and Petrology Group, Institute of Geosciences,
University of Leoben, Peter-Tunner-Str. 5, A-8700 Leoben, Austria

ABSTRACT

A combination of Raman spectrometry and microthermometry has been applied to synthetic fluid inclusions filled with pure H_2O, a NaCl brine and a $MgCl_2$ brine, in order to analyze spectra between –190° and +100°C. The combined technique allows: (1) the determination of the types of dissolved salts from the presence of salt hydrates at low temperatures, and (2) an accurate estimate of true temperatures of melting, even of phases that are difficult to observe within fluid inclusions. Raman spectra of water, brines, ice, glass and salt hydrates were analyzed by combined Gaussian–Lorentzian fitting of components. These fits illustrate the presence of singularities in the water spectra, around –35°C in a NaCl brine and around –30°C in a $MgCl_2$ brine. During freezing experiments, inclusions may contain different configurations of phases at the same temperature. Rapid freezing of a $MgCl_2$ brine inhibits the formation of a $MgCl_2$ hydrate, and in such inclusions, ice and supersaturated brine are present down to –190°C. The phase $MgCl_2$•$12H_2O$ forms only during slow cooling. Temperatures of phase changes, including eutectic point and final melting, were accurately determined by changes in measured Raman spectra of fluid inclusions. The variable freezing behavior of the same fluid inclusion, depending on cooling rates and cycling procedures, indicates the care with which natural fluid inclusions should be treated to obtain true salinities.

Keywords: Raman spectrometry, microthermometry, fluid inclusions, system H_2O–NaCl, system H_2O–$MgCl_2$.

SOMMAIRE

Une démarche combinée de spectrométrie de Raman et de microthermométrie a été appliquée à l'étude d'inclusions fluides synthétiques dans les systèmes H_2O, saumure à NaCl et saumure à $MgCl_2$, afin d'en analyser les spectres entre –190° et +100°C. Cette démarche mène à (1) la détermination des types de sels dissous selon la présence des hydrates des sels à faibles températures, et (2) une estimation juste des vraies températures de fusion, même des phases difficiles à observer dans les inclusions fluides. Les spectres de Raman pour l'eau, les saumures, la glace, un "verre" et les hydrates ont été analysés par simulations gaussiennes et lorentziennes des composantes. Ces simulations illustrent la présence de points singuliers dans le spectre de l'eau, près de –35°C dans la saumure à NaCl et près de –30°C dans la saumure à $MgCl_2$. Au cours des expériences cryométriques, les inclusions peuvent contenir des configurations différentes des phases à une seule température. Une congélation rapide d'une saumure à $MgCl_2$ entrave la formation de l'hydrate de $MgCl_2$, et dans de telles inclusions, la glace et une saumure sursaturée coexistent jusqu'à –190°C. La phase $MgCl_2$•$12H_2O$ ne cristallise que si le refroidissement est lent. Les températures des changements de phase, y inclus les points eutectiques et de fusion finale, ont été déterminées avec justesse selon les changements dans les spectres de Raman obtenus des inclusions fluides. Le comportement cryométrique variable d'une même inclusion, selon le taux de refroidissement et les procédures de cyclage des températures, souligne le soin nécessaire pour extraire une valeur fiable de la salinité de la phase fluide incluse.

(Traduit par la Rédaction)

Mots-clés: spectrométrie de Raman, microthermométrie, inclusions fluides, système H_2O–NaCl, système H_2O–$MgCl_2$.

§ *E-mail address*: bakker@unileoben.ac.at

Introduction

Raman spectroscopy is a powerful diagnostic tool in a wide variety of fields within geology (*e.g.,* Burke 2001). Moreover, Raman spectra can provide important insights into the structure and dynamics of stretching and bending of hydrogen bonds in pure water (*e.g.,* Ulness *et al.* 2001) and saline aqueous solutions. The analysis of salts and saline solutions is a major objective in the characterization of fluid inclusions. Estimations of salinity and ion ratios have been proven to be of major interest for the interpretation of many processes in diagenesis, metamorphism, and hydrothermal deposition of ore minerals (*e.g.,* Roedder 1984, Goldstein & Reynolds 1994). The aim of this study is to identify the Raman spectra of water, ice and specific solid salt hydrates, to determine the Gaussian and Lorentzian components, and to estimate the temperature dependence of its Raman shift. This work has previously been presented at the ECROFI XVI and PACROFI VIII meetings (Bakker 2001, 2002). In addition, the behavior of fluid inclusions containing brine at low temperatures can be documented precisely by Raman identification of the phases present. The development of Raman spectra from fluid inclusions during heating from low temperatures allows one to determine exactly those phase changes that define the salinity of the inclusions, and that are difficult to estimate optically.

Background Information

The existence of dissolved salts within fluid inclusions is inferred from the freezing-point depression of ice, or the presence of daughter crystals (*e.g.,* halite). These considerations might lead to estimations of salinity if one makes some basic presumptions. The types of anions and cations cannot be obtained directly from the freezing-point depression; therefore, the use of equivalent weight percentage NaCl was introduced as a reference value for solutions. [Note that weight (a force) is usually used as a synonym for mass, for which the SI unit is the kilogram. The term "mass %" should be used instead of "weight %" to indicate the salinity of an aqueous solution.] The measurement of first melting, *i.e.,* eutectic melting, peritectic melting and final melting of ice-like substances, is highly dependent on the quality of the microscope used. In principle, exact eutectic temperatures are impossible to detect because the initially small amount of liquid that appears at this temperature is not observable. The liquid phase is first noticeable at higher temperatures.

The Raman effect [see Ulness *et al.* (2001), and references therein for principles of Raman spectroscopy] is mainly achieved in material with covalent bonding. The energies of molecular vibrations, only for symmetrical stretching, are reflected in the wavelength of Raman scattered light. In material with ionic bonding, such as NaCl, only asymmetric stretching occurs. It results in no overall change in polarizability, and no Raman-active modes are observed. Dissolved simple ions, such as Na^+ and Cl^- are, by definition not Raman-active because chemical bonding is not present (Lilley 1973). This fact makes Raman spectroscopy ineffective for the analysis of dissolved salt species in fluid inclusions.

In fluid-inclusion research, Raman spectroscopy is mainly applied to identify qualitatively gases in vapor bubbles and entrapped solid phases (*e.g.,* Burke 2001). The Raman spectra of H_2O and aqueous solutions were characterized by Walrafen (1972), Lilley (1973) and Sceats & Rice (1982), among others. The OH-stretching mode of H_2O has a broad band of several hundred wavenumbers, with a principal peak at 3415 ± 5 cm^{-1}, a shoulder at 3625 ± 10 cm^{-1}, and a weak broad shoulder at 3275 cm^{-1} (Walrafen 1972). The temperature-dependent shape of the raw spectrum of H_2O has been studied purely morphologically by Frantz *et al.* (1993), who described up to six inflection points between 100 and 505°C, 23 and 202 MPa. Individual Gaussian components were not identified in their study.

The morphology of the spectrum of water at room temperature is modified by the presence of dissolved salts. The change in shape with increasing salinity was studied purely morphologically by Mernagh & Wilde (1989) and Dubessy *et al.* (1997). Their method includes an arbitrary integration of two halves of the raw spectrum, from 2800 to 3300 cm^{-1} and from 3300 to 3800 cm^{-1}, which then define a "skewing parameter". This method does not allow a specification of both dissolved anions and cations, and the integration boundaries have no physical meaning. Again, individual Gaussian components were not identified.

In order to identify the type of salt species present in fluid inclusions, Dubessy *et al.* (1982) introduced the use of cryogenic Raman measurements on electrolyte-bearing solutions. At low temperatures, any dissolved salt in aqueous solutions may form a solid salt-hydrate, which is Raman-active. Falk & Knop (1973) had already illustrated the peak positions of several salt-hydrates from isotopically diluted solutions, including $NaCl•2H_2O$ and $MgCl_2•6H_2O$, and their variation with temperature. Remarkably few studies in fluid-inclusion research have been presented since then, although the identification of dissolved ions has become a study of major importance. Samson & Walker (2000) have recently reinforced the usefulness of the combined technique of microthermometry and Raman spectroscopy. The advantage of this combination is two-fold: 1) determination of the type of dissolved salt from the presence of solid salt-hydrate at low temperatures, and 2) accurate estimate of true melting temperatures of phases that are difficult to observe.

Analytical Methods

Fluid inclusions were synthesized according to the experimental method described by Bodnar & Sterner

(1987). Solutions of pure H_2O, 23.2 mass % NaCl and 20.2 mass % $MgCl_2$ were included individually as fluid inclusions in three cores of natural quartz during crack-healing at approximately 600°C and 200 MPa.

Raman spectroscopic measurements were done with a LABRAM (ISA Jobin Yvon) instrument using a frequency-doubled Nd–YAG laser (100 mW source). Wavenumber measurements have an accuracy of 1.62 cm^{-1} at low $\Delta\nu$ (Raman shift around 0 cm^{-1}) and 1.1 cm^{-1} at high $\Delta\nu$ (around 3000 cm^{-1}). Microthermometry was conducted with a Linkam THMSG 600 heating–freezing stage; an Olympus 100× long-working-distance objective (LMPlanFI, 0.80 numerical aperture) has been used. The stage was calibrated using synthetic fluid inclusions at –56.6, 0.0, and 374.0°C, *i.e.,* melting of pure CO_2, melting of pure H_2O and critical homogenization of pure H_2O, respectively. Raman spectra of fluid inclusions were measured in a time span of 20 seconds at selected temperatures, in intervals of 10°C. During the freezing experiments, a vapor phase remained present within all the fluid inclusions. Each Raman measurement was performed at approximately the same spot within the inclusion. Slight displacement of the focus spot may have important effects on the absolute intensity of Raman spectra. Subsequently, at each selected temperature, the background spectrum of the quartz host was measured, and subtracted from the signal produced by the inclusion (Fig. 1). The resulting spectra were analyzed by the peak-fitting program PeakFit, v. 4.11 (© SYSTAT Software Inc.) to estimate the peak position (p), half-width (w), amplitude (a) and fraction of Gauss function (g) in Gaussian–Lorentzian contributions:

$$y = a\left[\frac{g\frac{\sqrt{\ln(2)}}{w\sqrt{\pi}}\exp\left\{-4\cdot\ln(2)\cdot q^2\right\} + (1-g)\frac{1}{\pi\cdot w\left\{1+4\cdot q^2\right\}}}{g\frac{\sqrt{\ln(2)}}{w\sqrt{\pi}} + (1-g)\frac{1}{\pi\cdot w}}\right] \quad (1a)$$

$$q = \frac{x-p}{w} \quad (1b)$$

where x is the Raman shift $\Delta\nu$ (*i.e.,* wavenumber in cm^{-1}), and y is the corresponding intensity of the Raman spectrum. The fraction g was defined as a smoothing function (sigmoid) of temperature, whereas p, w and a were mainly defined as polynomial functions of temperature.

Raman Spectra of Synthetic Fluid Inclusions

The quality of the Raman spectra of water, salt hydrates and ice-like phases is temperature- and crystallinity-dependent. At very low temperatures, *e.g.,* at –190°C, peaks of ice and hydrates are well defined, with narrow half-width values. At higher temperatures, the position and shape of some peaks change, and become less pronounced, as the spectrum begins to resemble a widely broadened spectrum of liquid H_2O.

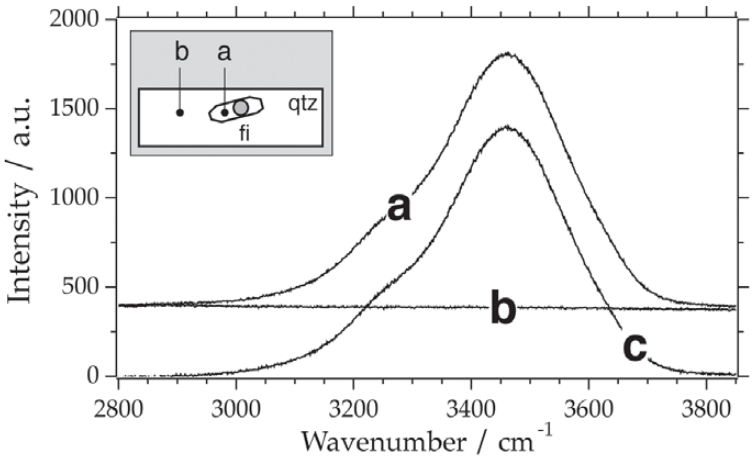

FIG. 1. Method of background correction: Raman spectra of water within a fluid inclusion (a), quartz signal at the same level (b), and the differential resulting spectrum (c) used for fitting procedure of Gaussian–Lorentzian contributions.

H_2O

In aqueous fluid inclusions about 20 μm in diameter, the nucleation temperature of ice during cooling experiments is about –35 to –40°C. This metastability enables the measurement of H_2O (liquid) well below the melting temperature of pure ice. The properties of water were analyzed by Raman spectrometry in the range from –40° to +100°C. Ice (phase structure Ih) has been measured in the range from –190° to 0°C.

The spectrum of water consists of three Gaussian–Lorentzian contributions (Fig. 2a), which change in shape, position and relative intensity with temperature (Figs. 2b, 3, Appendix Tables A1–A4). At 20°C, the peaks are positioned at 3222 ($\Delta\nu_2^{liq}$), 3433 ($\Delta\nu_1^{liq}$) and 3617 cm^{-1} ($\Delta\nu_3^{liq}$), each corresponding to specific stretching modes of water. Peak $\Delta\nu_2^{liq}$ has the highest intensity at –35°C, whereas at 100°C, peak $\Delta\nu_1^{liq}$ is dominant (Figs. 2b, 3d). The position of both $\Delta\nu_1^{liq}$ and $\Delta\nu_2^{liq}$ and their half-width values change sharply to lower values toward –40°C (Figs. 3a, b). Peak $\Delta\nu_3^{liq}$ nearly disappears toward lower temperatures.

Ice has a Raman spectrum significantly different from that of water, with a more intense signal and a clearly defined narrow main peak (Fig. 4a). The complex spectrum obtained at –190°C consists of six Gaussian–Lorentzian contributions, corresponding to specific OH-stretching modes of ice. At –190°C, ice has two main peaks, at 3102 ($\Delta\nu_1^{ice}$) and 3225 cm^{-1} ($\Delta\nu_2^{ice}$). The intensity of $\Delta\nu_1^{ice}$ is always a factor of 15 higher than $\Delta\nu_2^{ice}$ (Fig. 5c). In addition, three minor peaks are positioned at 3005 ($\Delta\nu_3^{ice}$), 3338 ($\Delta\nu_4^{ice}$) and 3414 cm^{-1} ($\Delta\nu_5^{ice}$). The peak at 3255 cm^{-1} ($\Delta\nu_6^{ice}$) has a broad half-width value with a relative low intensity, which forms a kind of background stretching mode of the ice structure. The spectrum of ice clearly has a shift in peak positions and shape between temperatures of –190° and 0°C (Figs. 4b, 5). The absolute intensity of the Raman spectrum clearly decreases with increasing temperature, as it begins to resemble the spectrum of water (*cf.* Figs. 2b, 3b). All Gaussian–Lorentzian contributions shift to higher wavenumbers and higher half-width values with increasing temperature (Figs. 5a, b, Appendix Tables B1–B4). The uncertainty of peak position and half width of $\Delta\nu_2^{ice}$ increases toward the final melting point of ice, as it becomes less pronounced.

H_2O–NaCl

Freezing experiments with inclusions containing a 23.2 mass % NaCl solution (Fig. 6) illustrate a different phase-change behavior than inclusions containing pure H_2O. First, rapid cooling causes the nucleation of a saline glass-like substance at about –82°C, which is mainly noticeable by deformation of the vapor bubble, but not by textural or color changes of the liquid phase. This glass-like solid remains present down to temperatures of –190°C. During subsequent heating, this phase assemblage remains stable up to –25°C (Fig. 6b at –60°C), where this glass-like material recrystallizes to a randomly oriented microcrystalline mixture of ice and hydrohalite, which has a granular texture and a brownish color. This assemblage represents a stable configuration, even after subsequently cooling down to –190°C (Fig. 6c at –60°C). During further heating, single crystals of hydrohalite, with a greenish color, can be grown in a saline aqueous liquid solution slightly above the eutectic point, *i.e.,* –21.2°C. Cooling this assemblage results in the growth of those hydrohalite crystals in a metastable brine (Fig. 6d at –60°C) and the nucleation of a glass-like substance from the remaining less saline aqueous solution at around –65°C. This phase assemblage with a less saline glass behaves similarly to the glass previously described in Figure 6b, and can also be observed at –60°C (Fig. 6e). It also recrystallizes a few degrees below the eutectic temperature. After temperature cycling, larger crystals of hydrohalite and ice can be cultivated (Fig. 6f). As illustrated in Figure 6, at –60°C, four different phase-assemblages can be present in the fluid inclusions, depending on specific heating–freezing procedures.

At 20°C, the Raman spectrum of the NaCl brine (Fig. 7a) is slightly different from that of pure water. The two main Gaussian–Lorentzian contributions are shifted to higher wavenumbers, 3456 ($\Delta\nu_1^{aq}$) and 3263 cm^{-1} ($\Delta\nu_2^{aq}$). The third contribution has a similar position of the peak, 3618 cm^{-1} ($\Delta\nu_3^{aq}$), and forms a weak shoulder. The peak positions are relatively stable with temperature (Figs. 7b, 8, Appendix Tables C1–C4), and shift about half of that for pure H_2O. The main peak ($\Delta\nu_1^{aq}$) remains dominant within the temperature interval of –80°C to +100°C (Figs. 7, 8). The trend in temperature dependence of peak position, half-width and intensities of all contributions is significantly different below and above –35°C (Fig. 8), which represents a basic change in the structure of the brine. Below –35°C, both peak position and half-width values change rapidly with temperature, whereas above –35°C, those values are less sensitive to temperature changes. A fragment of this behavior is observed in fluid inclusions containing pure H_2O (Fig. 3), as illustrated by the steep change in peak position toward the nucleation temperature around –35°C. The apparent phase-change is not reached in those inclusions because it occurs below the ice-nucleation temperature.

The previously mentioned microcrystalline mixture (Fig. 6c) has a combined Raman spectrum with randomly oriented hydrohalite and ice microcrystals (Fig. 9). The position of the Raman peaks of ice is slightly influenced by the presence of hydrohalite in the microcrystalline mixture. The main peak of ice is shifted about 5 wavenumbers, from 3104 to 3099 cm^{-1} at –190°C. There is no measurable effect on the shapes of the peaks of ice. The spectrum of ice is subtracted to

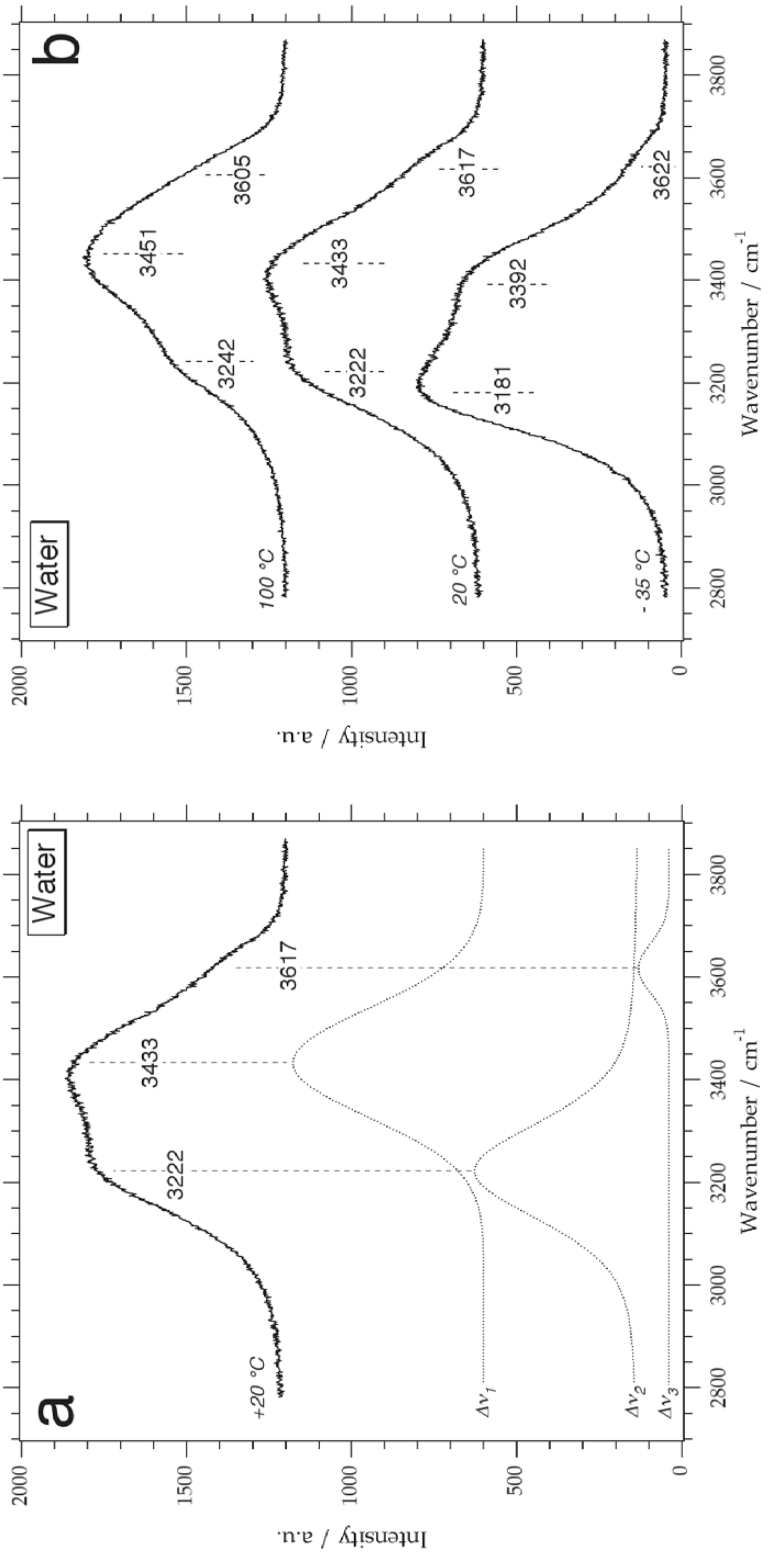

FIG. 2. (a) Raman spectrum of water at 20°C with three Gaussian–Lorentzian contributions, $\Delta\nu_1^{liq}$, $\Delta\nu_2^{liq}$ and $\Delta\nu_3^{liq}$. (b) Raman spectra of water at +100°, +20° and –35°C, illustrating the shift of Gaussian–Lorentzian contributions with temperature.

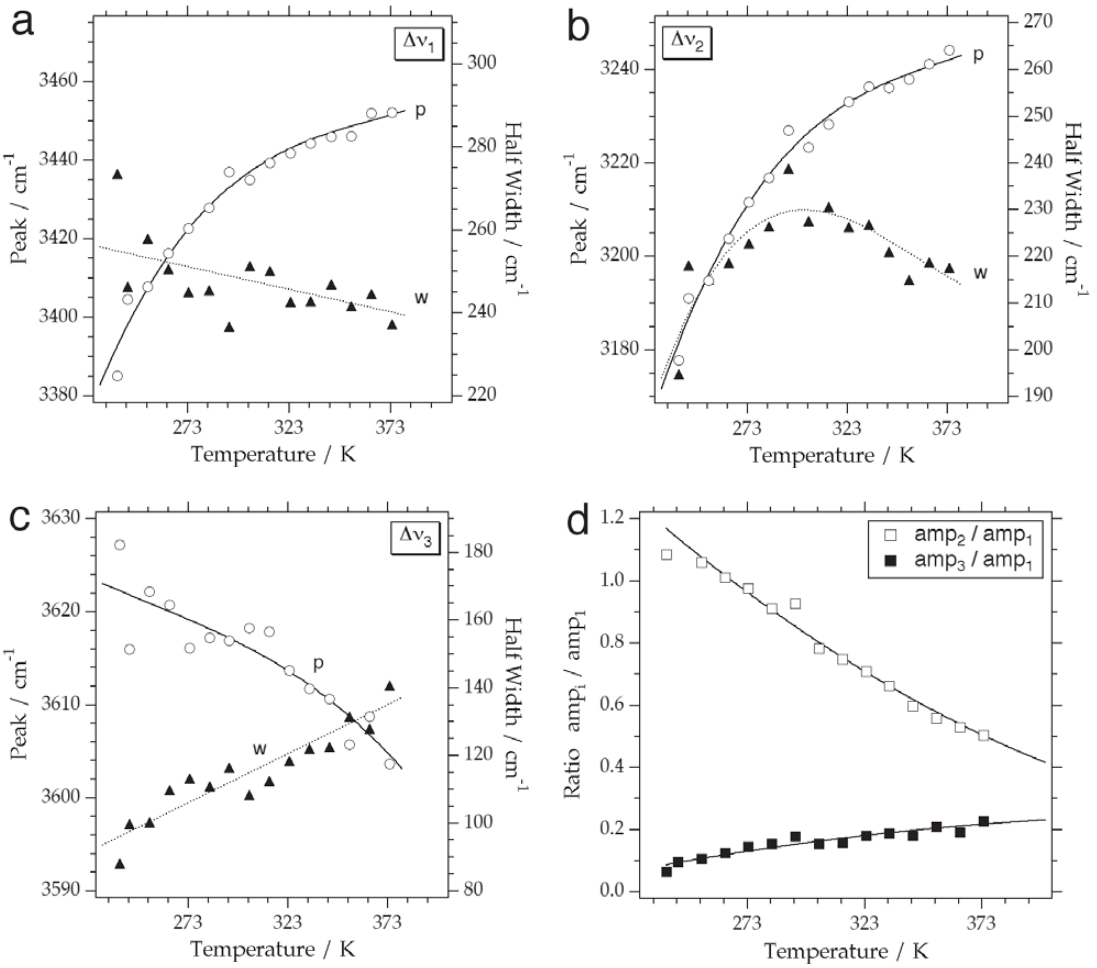

FIG. 3. Temperature dependence of peak position (open circles) and half-width (solid triangles) of $\Delta\nu_1^{liq}$ (a), $\Delta\nu_2^{liq}$ (b) and $\Delta\nu_3^{liq}$ (c) of water. The letters p and w indicate the best-fit curves for peak position and half width, respectively. The relative intensities of $\Delta\nu_2^{liq}$ and $\Delta\nu_3^{liq}$ are indicated as a ratio to $\Delta\nu_1^{liq}$ (d).

obtain a signal purely attributable to the hydrohalite (Fig. 10a), similar to the subtraction of the background signal in Figure 1. The Raman spectrum of hydrohalite has five well-defined Gaussian–Lorentzian components, which peaks remain at approximately constant position in the temperature interval from –190° to –30°C (Figs. 10b, 11, Appendix Tables D1–D4). The peaks are shifted by a maximum of 8 cm^{-1} in this temperature range. The main peak is at 3424 cm^{-1} ($\Delta\nu_1^{hh}$) at –190°C, with two shoulder peaks at 3407 ($\Delta\nu_2^{hh}$) and 3439 cm^{-1} ($\Delta\nu_4^{hh}$). A second major peak occurs at 3539 cm^{-1} ($\Delta\nu_3^{hh}$). A minor peak is present at 3326 cm^{-1} ($\Delta\nu_5^{hh}$). A sixth Gaussian–Lorentzian function ($\Delta\nu_6^{hh}$) forms a background OH-stretching mode of the hydrohalite crystals with a broad half-width value, and a relatively low intensity, similar to that of ice. At higher temperatures, individual peaks become less well pronounced, and are combined in a single smoothed Raman peak-shape with a broad half-width value (Fig. 10b).

The randomly oriented grains in the microcrystalline mixture in the fluid inclusion (Fig. 6c) produce an average spectrum. Consequently, the relative intensities of the peaks are invariant at a selected temperature. Growing large single crystals of hydrohalite may result in a change in relative intensities, as suspected from the crystallographic-orientation-dependent Raman effect. For example, the hydrohalite spectrum illustrated by Dubessy *et al.* (1982) has a major peak at 3406 cm^{-1}, which is only the second most intense peak in this study, *i.e.,* $\Delta\nu_2^{hh}$.

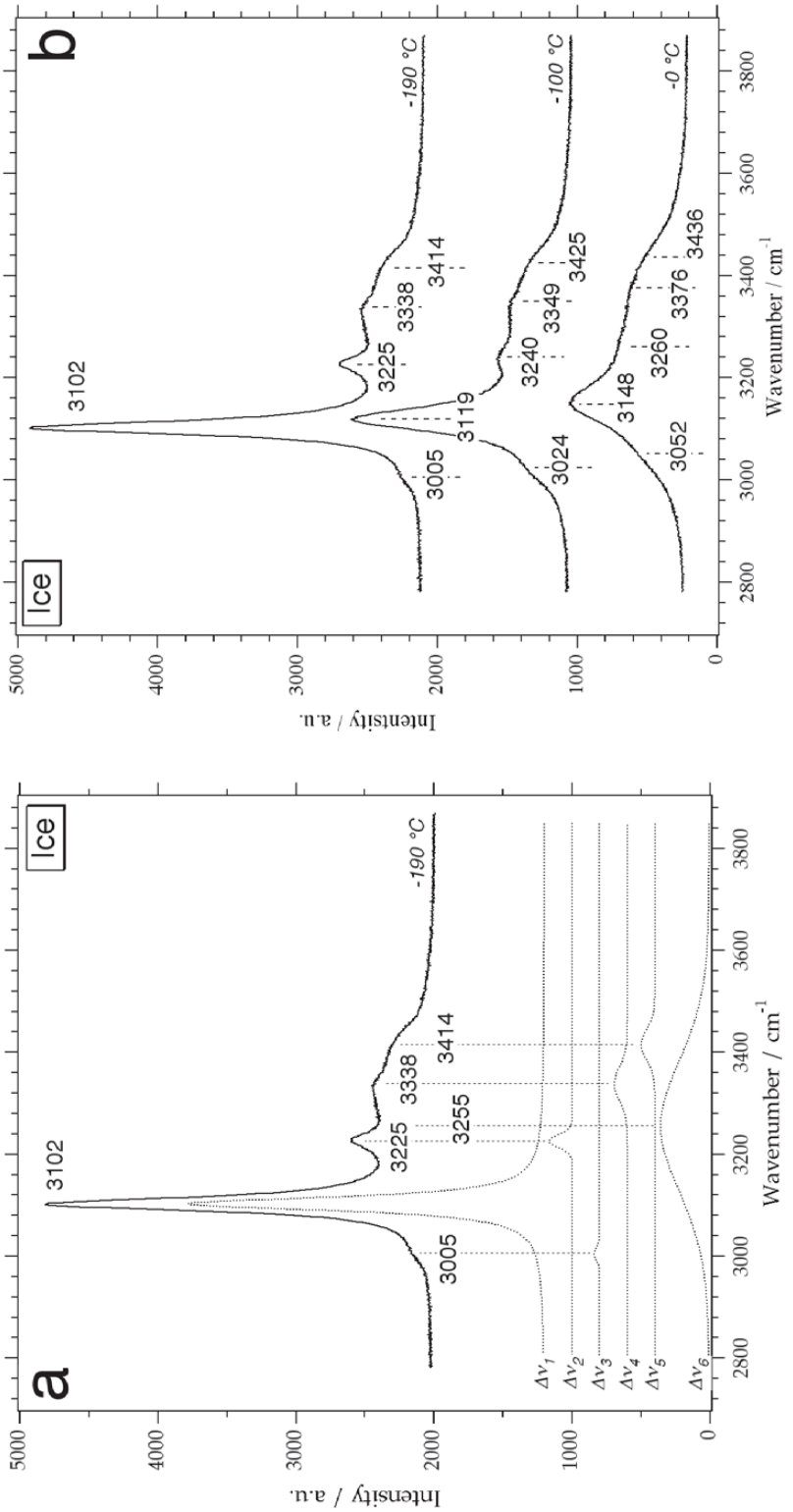

FIG. 4. (a) Raman spectrum of ice at −190°C with six Gaussian–Lorentzian contributions, $\Delta\nu_1^{ice}$, $\Delta\nu_2^{ice}$ and $\Delta\nu_3^{ice}$, $\Delta\nu_4^{ice}$, $\Delta\nu_5^{ice}$ and $\Delta\nu_6^{ice}$. (b) Raman spectra of ice at −190°, −100° and 0°C, illustrating the shift of Gaussian–Lorentzian contributions with temperature.

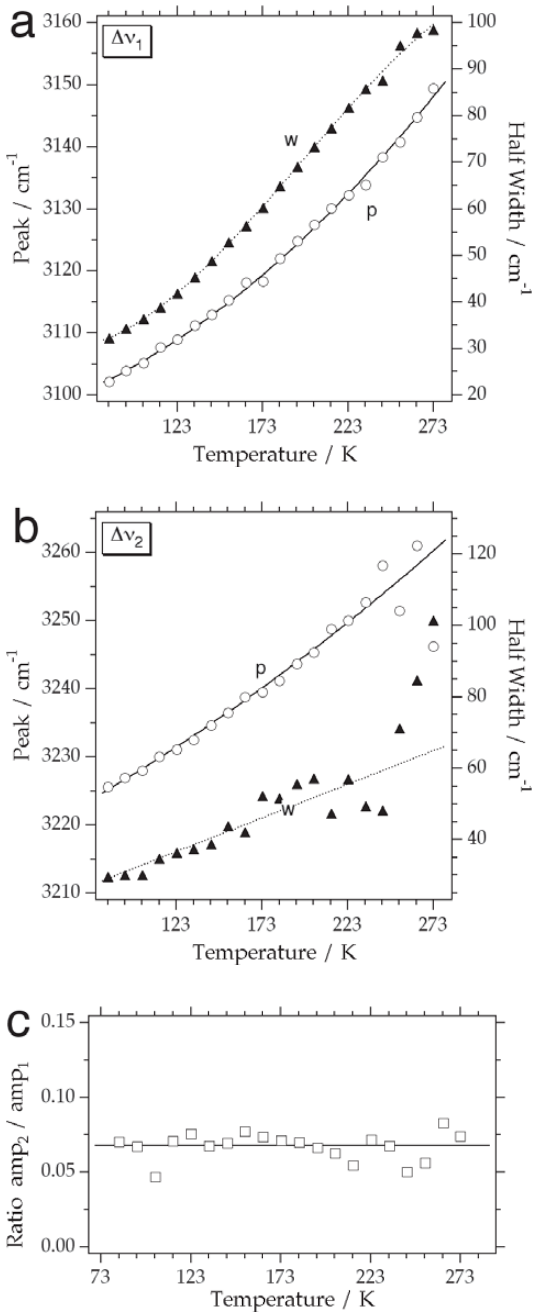

FIG. 5. Temperature dependence of the two main peak positions (open circles) and half-width (solid triangles) of $\Delta\nu_1^{ice}$ (a), $\Delta\nu_2^{ice}$ (b) of ice. The letters p and w indicate the best-fit curves for peak position and half width, respectively. The relative intensity of $\Delta\nu_2^{ice}$ is indicated as a ratio to $\Delta\nu_1^{ice}$ (c).

The Raman spectrum of the NaCl-glass-like material (Fig. 6b), which formed in the inclusion directly after rapid cooling, has many similarities to that for a mixture of ice and hydrohalite (Fig. 12). However, at –190°C, the position of the main peak of ice has shifted to even lower values, *i.e.,* 3096 cm^{-1}, differing by about 8 cm^{-1} from that of pure ice. Those peaks belonging to a hydrohalite structure are less intense than those of ice, with broader half-width values. The absolute intensity of the spectrum for the glass is much lower than that of the microcrystalline mixture of hydrohalite.

H_2O–$MgCl_2$

The freezing behavior of a 20.2 mass % $MgCl_2$ solution in fluid inclusions (Fig. 13) is significantly different from that of the pure water and the NaCl solution just described. Rapid cooling to –190°C causes the formation of a saline glass in the presence of a few small crystals of ice. These ice crystals grew extremely slowly down to about –90°C, and stopped as the glass nucleated at this temperature. This nucleation is not noticeable by deformation of the vapor bubble. This configuration remained present in the inclusions down to –190°C (Fig. 13b at –120°C). Subsequent heating of this assemblage to about –110°C results in its recrystallization to a multicrystalline mixture of ice and a film of supersaturated brine between individual grains. $MgCl_2$ hydrate is not formed during this process. In this assemblage, large single crystals of ice can be obtained after cooling from nearly the final melting temperature of ice (Fig. 13c at –120°C). By either rapid or slow cooling, these ice crystals grow down to about –75° to –70°C in the presence of a brine and a vapor bubble. Further cooling does not change the volumetric proportion of the phases present, *i.e.,* 41 vol.% brine, 38 vol.% ice and 21 vol.% vapor bubble (Fig. 14). Consequently, a supersaturated brine remains present as a liquid phase even down to –190°C. $MgCl_2$ hydrate can only be grown by initial slow cooling from room temperatures. A slow nucleation of ice and $MgCl_2 \cdot 12H_2O$ occurs between –70° and –90°C. Fewer crystals nucleate, and these become larger than those of hydrohalite grown from a NaCl brine (see previous paragraph). This crystalline mixture remains stable between –190° and –33°C (Fig. 13d at –120°C), *i.e.,* the eutectic temperature in the binary fluid system H_2O–$MgCl_2$. As illustrated in Figure 13, the fluid inclusion may contain three different phase-configurations at –120°C, depending on the freezing–

FIG. 6. A synthetic fluid inclusion with a 23.2 mass % NaCl solution at selected temperatures: +20° (a), –60° (b, c, d, e) and –22°C (f). See text for further details.

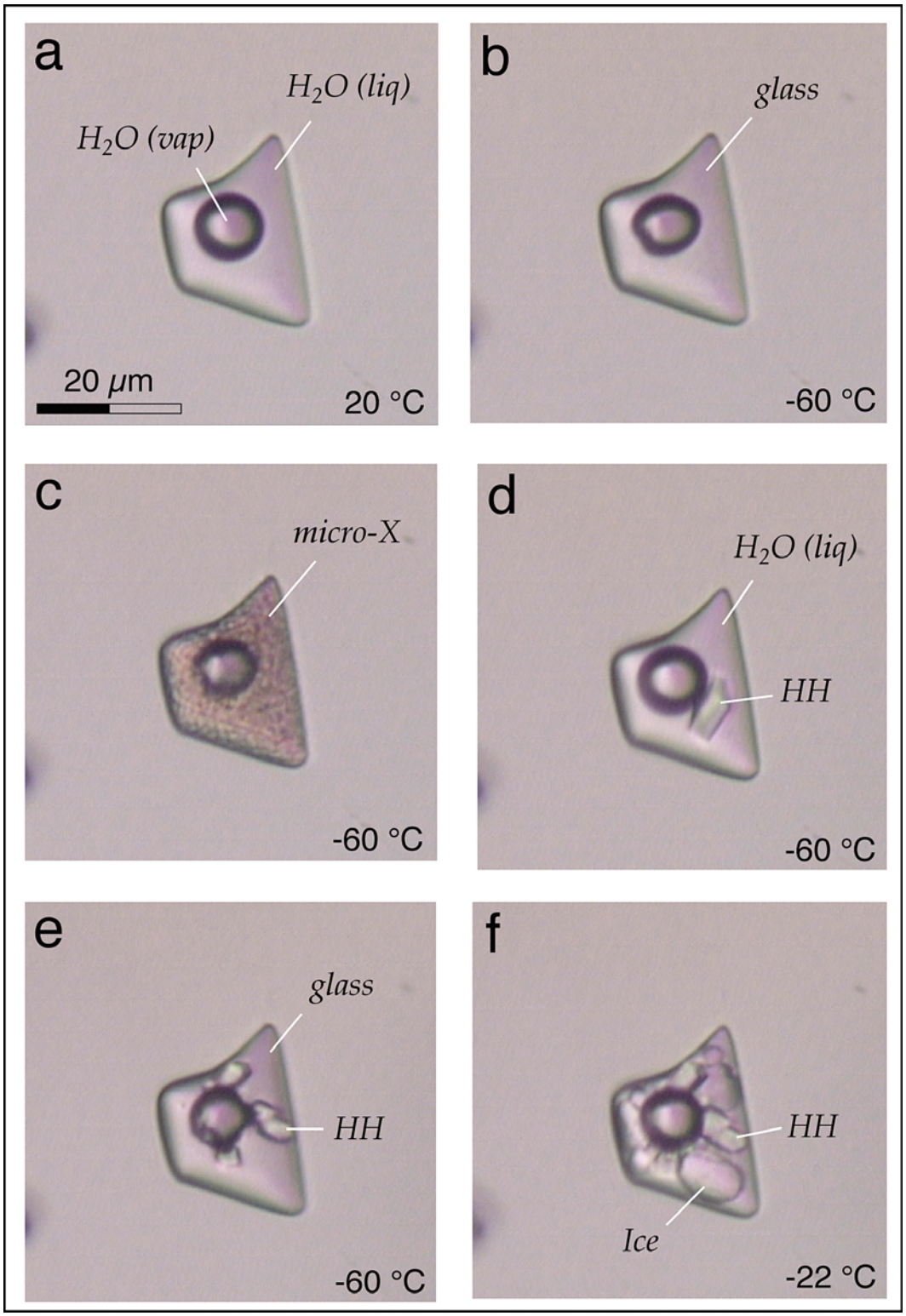
a
H_2O (liq)
H_2O (vap)
20 μm
20 °C
b
glass
-60 °C
c
micro-X
-60 °C
d
H_2O (liq)
HH
-60 °C
e
glass
HH
-60 °C
f
HH
Ice
-22 °C

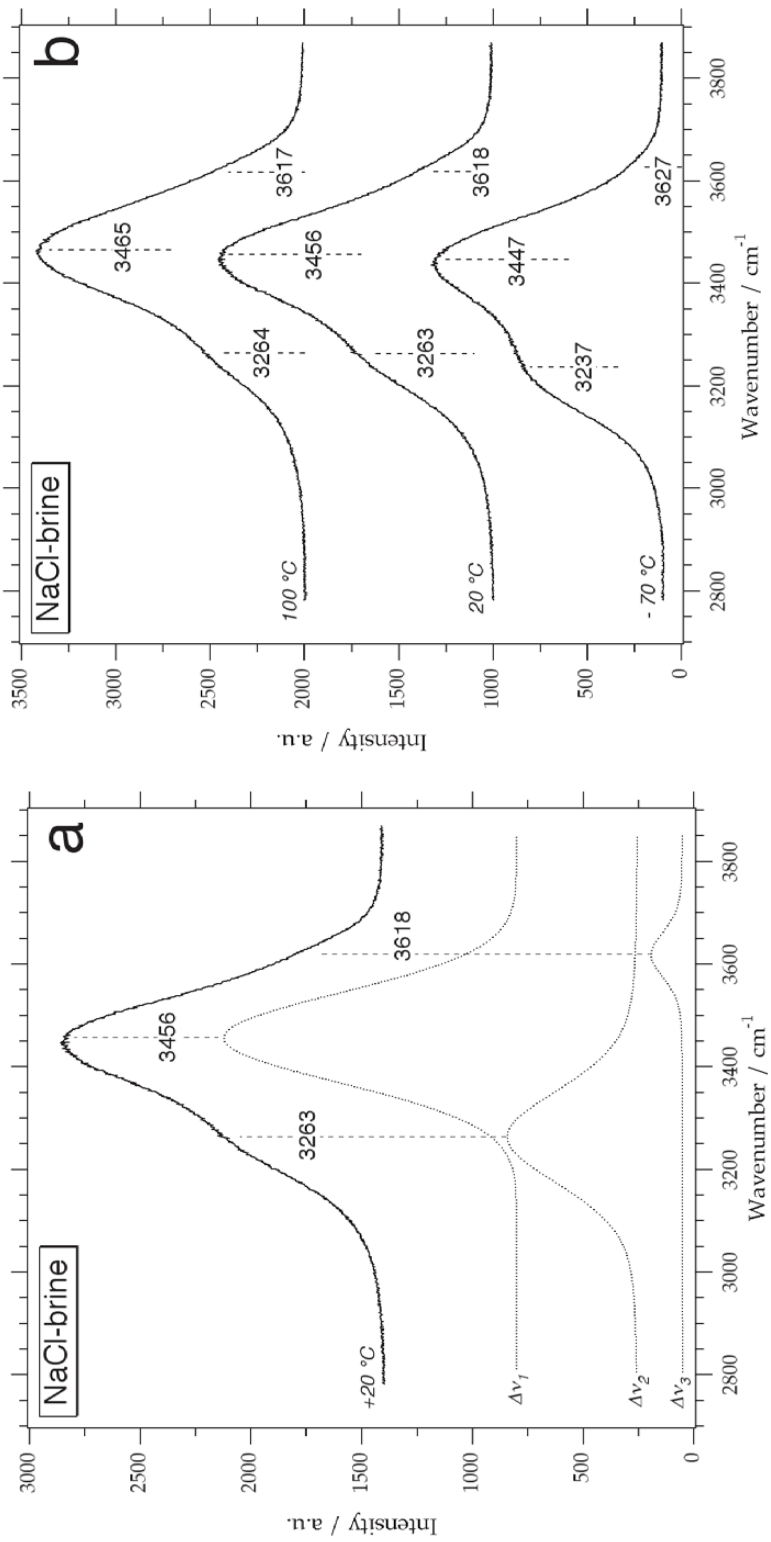

FIG. 7. (a) Raman spectrum of NaCl brine at 20°C with three Gaussian–Lorentzian contributions, $\Delta\nu_1^{aq}$, $\Delta\nu_2^{aq}$ and $\Delta\nu_3^{aq}$. (b) Raman spectra of this brine at +100°, +20° and –70°C, illustrating the shift of Gaussian–Lorentzian contributions with temperature.

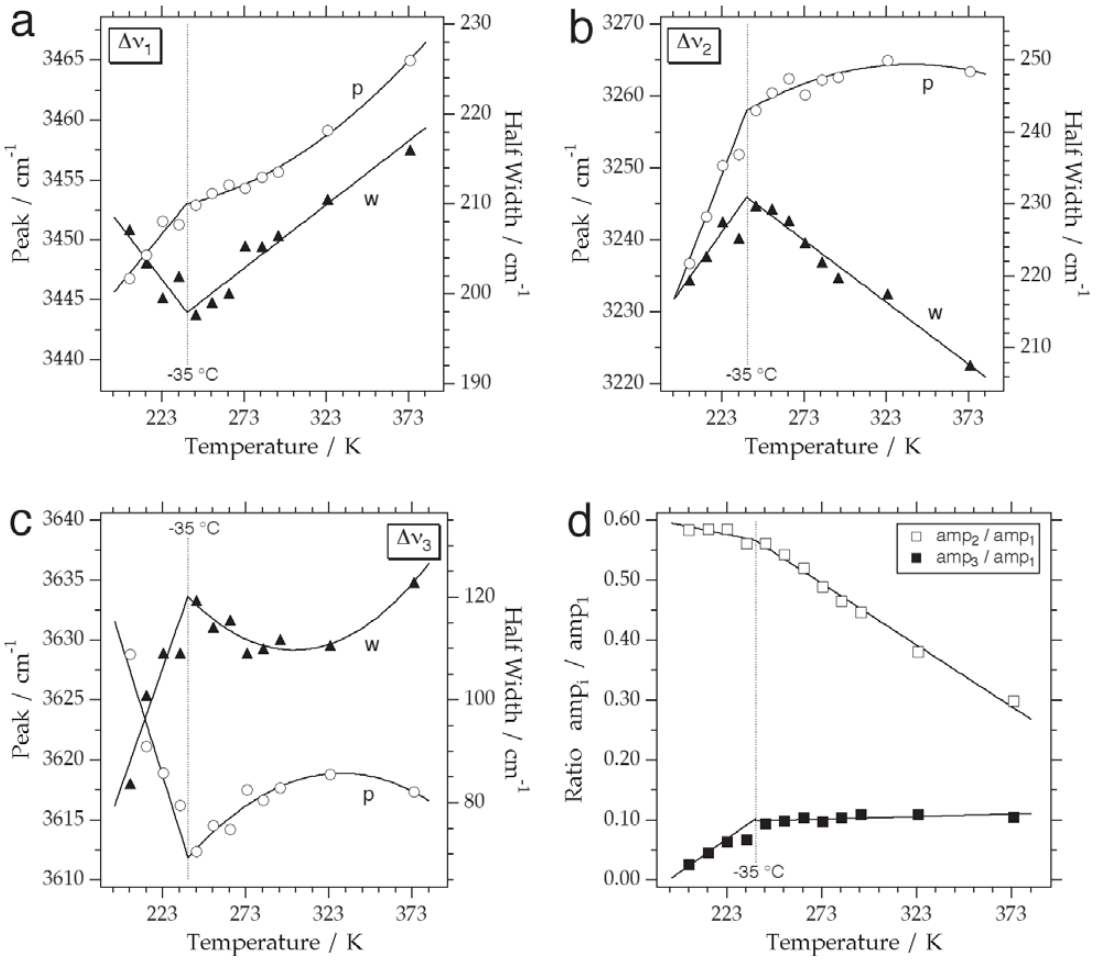

FIG. 8. Temperature dependence of peak position (open circles) and half width (solid triangles) of $\Delta\nu_1^{aq}$ (a), $\Delta\nu_2^{aq}$ (b) and $\Delta\nu_3^{aq}$ (c) of the NaCl brine. The letters p and w indicate the best-fit curves for peak position and half width, respectively. The relative intensities of $\Delta\nu_2^{aq}$ and $\Delta\nu_3^{aq}$ are indicated as a ratio to $\Delta\nu_1^{aq}$ (d).

heating procedure performed. The configuration of multicrystalline ice, $MgCl_2 \cdot 12H_2O$ and a vapor bubble represents a stable phase-assemblage (Fig. 13d).

The Raman spectrum of a 20.2 mass % $MgCl_2$ brine in the presence of only a vapor bubble is apparently similar to a NaCl brine and consists of three Gaussian–Lorentzian contributions within the temperature range of –85° to +100°C (Fig. 15). The main peak is positioned at 3448 cm^{-1} ($\Delta\nu_1^{aq}$) at 20°C, which is about 8 cm^{-1} lower than for a NaCl brine (*cf.* Fig. 7a). Similarly, the second peak at 3273 cm^{-1} ($\Delta\nu_2^{aq}$) is shifted by 10 cm^{-1}, in the opposite direction, however. The third peak, 3594 cm^{-1} ($\Delta\nu_3^{aq}$) is shifted by about 24 cm^{-1} to lower values compared to a NaCl brine (*cf.* Fig. 7a). The main peak $\Delta\nu_1^{aq}$ remains the most intense one within the temperature interval indicated. The trends of all Raman peaks with temperature change drastically close to –30°C (open circles in Fig. 16, Appendix Tables E1–E4). Peak position, half-width value and trends in relative intensity are significantly different on either side of this temperature. A similar behavior is observed with a NaCl brine around –35°C (Fig. 8).

The temperature-dependent behavior of the Raman spectrum of a $MgCl_2$-rich brine in the presence of both a vapor bubble and ice is significantly different. Below –30°C, measurement of the liquid phase could be performed even down to –190°C, as it is stabilized by the presence of ice crystals. At –190°C, the brine has a salinity of approximately 39 mass % $MgCl_2$ in the presence of pure ice, as obtained from the estimates of

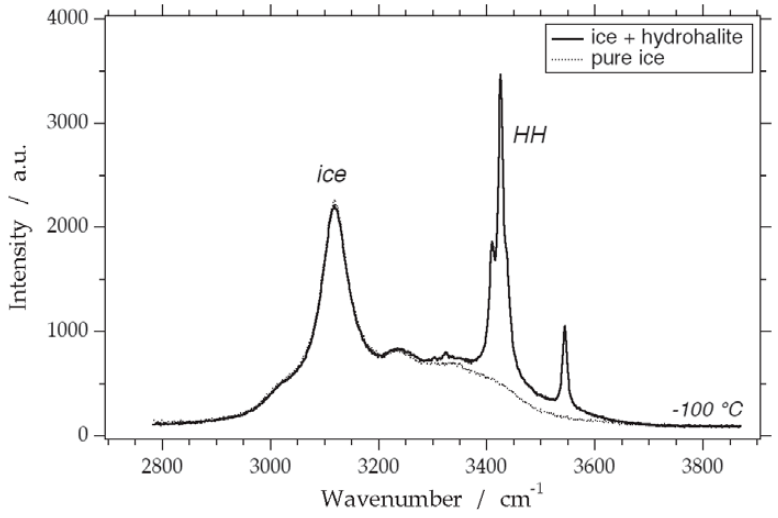

FIG. 9. Raman spectrum of a frozen synthetic fluid inclusions at –100°C with a combination of ice and hydrohalite peaks. The dashed curve is a Raman spectrum of pure ice, which is subtracted to obtain a signal resulting from hydrohalite only. HH: hydrohalite.

volume fractions (Fig. 14). The shape of the Raman spectrum of the supersaturated brine at –190°C (Fig. 17) resembles the spectrum of the saturated brine at 20°C in the presence of only a vapor bubble (Fig. 15). Up to –70°C, only small changes occur in volumetric properties of the inclusions, which is reflected in nearly constant Gaussian–Lorentzian contributions of the Raman spectrum. The position of the main and second peak remains relatively constant, at 3434 to 3430 cm^{-1} ($\Delta\nu_1^{aq}$) and 3288 to 3300 cm^{-1} ($\Delta\nu_2^{aq}$) in a temperature interval between –190° and –70°C (Fig. 16, Appendix Tables F1–F4). At –70°C, the ice starts to melt, until the final melting temperature of ice is reached at –30.5°C. Within this melting interval, the Raman spectrum of the brine is rapidly changing (Fig. 16), as temperature and salinity are constantly changing. At the final melting temperature of ice, the Raman spectra are similar to those described in the previous paragraph.

The position of Raman peaks of ice is affected by the presence of a $MgCl_2$ brine or solid $MgCl_2$•$12H_2O$ (Fig. 18). Most of the six peaks of ice are shifted approximately 9 cm^{-1} to lower wavenumbers. Toward higher temperatures, the peaks of ice more closely resemble those in the Raman spectrum of pure ice. Single crystals of $MgCl_2$ hydrate could not be cultivated in the freezing experiments, nor was a microcrystalline mixture formed (*cf.* hydrohalite in Fig. 6). Freezing experiments invariably resulted in a mixture of coarsely crystalline $MgCl_2$•$12H_2O$ and ice (see Fig. 13d). Consequently, the orientation of those crystals of $MgCl_2$ hydrate may generate a variety of intensities for individual peaks at a selected temperature (Fig. 19), whereas the peak position and half-width values remain constant. To obtain a signal originating from $MgCl_2$•$12H_2O$ only, the spectrum of ice was subtracted from the observed Raman spectrum (Fig. 20). The resulting Raman spectrum of $MgCl_2$•$12H_2O$ has seven well-defined Gaussian–Lorentzian components (Fig. 21a). The main peaks are positioned at 3517 ($\Delta\nu_1^{mh}$), 3465 ($\Delta\nu_2^{mh}$) and 3404 cm^{-1} ($\Delta\nu_3^{mh}$). The peak at 3199 cm^{-1} ($\Delta\nu_4^{mh}$) nearly coincides with the second peak of ice. Minor peaks are positioned at 3324 ($\Delta\nu_6^{mh}$), 3437 ($\Delta\nu_6^{mh}$) and 3483 cm^{-1} ($\Delta\nu_7^{mh}$). An eight Gaussian–Lorentzian function ($\Delta\nu_8^{mh}$) forms a background OH-stretching mode of the $MgCl_2$ hydrate crystals with a broad half-width value, and a relative low intensity. As with hydrohalite, the peak positions change by only a small amount in the temperature interval from –190° to –50°C (Figs. 21b and 22, Appendix Tables G1–G4). Individual peaks become less well pronounced at higher temperatures, as the spectrum changes to a smoothed less intense Raman signal with a broad half-width value (Fig. 21b).

After rapid cooling of fluid inclusions, a saline "glass-like" substance may form in the presence of a few small crystals of ice (Fig. 13b). At –190°C, the Raman spectrum of this glass is substantially different from the spectrum of the supersaturated brine presented in the previous paragraph, and is very unlike the spectrum of a glass formed at the expense of a NaCl-rich brine (*cf.* Figs. 17, 23). The glass spectrum has been measured in the temperature range from –190° to –110°C, at which point it recrystallizes to ice crystals and a brine. The spectrum contains five Gaussian–Lorentzian components (Fig. 23) and is nearly tempera-

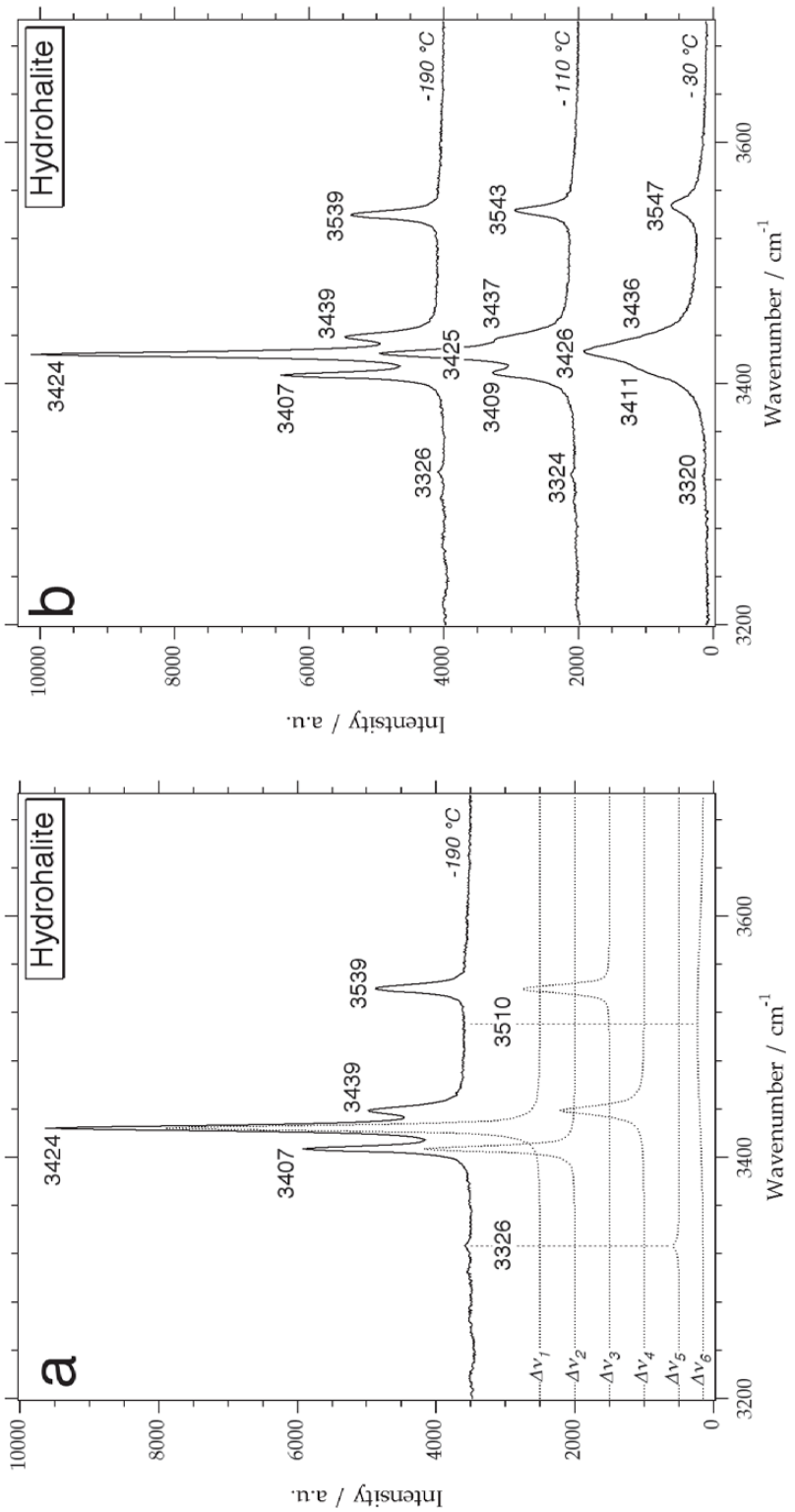

FIG. 10. (a) Raman spectrum of hydrohalite at –190°C with six Gaussian–Lorentzian contributions, $\Delta\nu_1^{hh}$, $\Delta\nu_2^{hh}$ and $\Delta\nu_3^{hh}$, $\Delta\nu_4^{hh}$, $\Delta\nu_5^{hh}$ and $\Delta\nu_6^{hh}$. (b) Raman spectra of hydrohalite at –190°, –110° and –30°C, illustrating the shift of Gaussian–Lorentzian contributions with temperature.

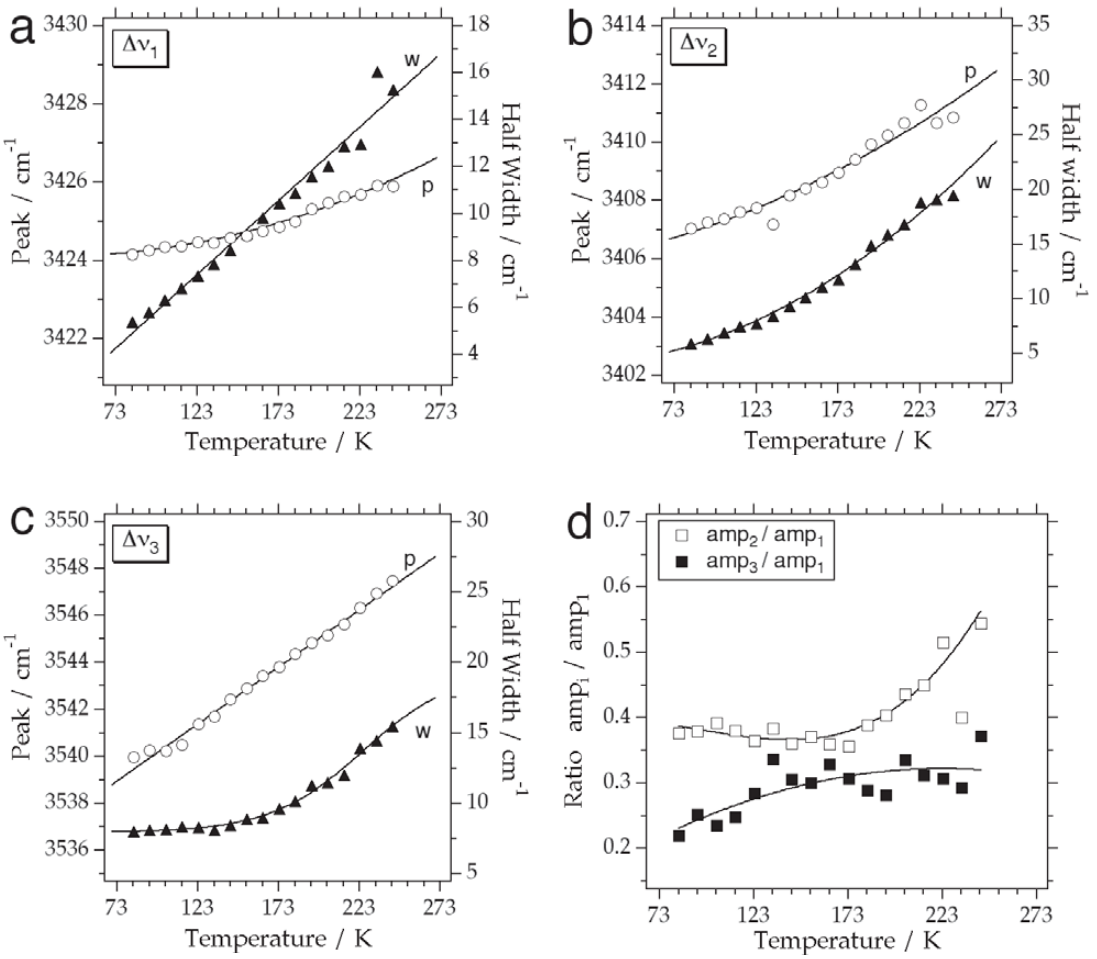

FIG. 11. Temperature dependence of the three main peak positions (open circles) and half-width (solid triangles, of $\Delta\nu_1^{hh}$ (a), $\Delta\nu_2^{hh}$ (b) and $\Delta\nu_3^{hh}$ (c) of hydrohalite. The letters p and w indicate the best-fit curves for peak position and half width, respectively. The relative intensities of $\Delta\nu_2^{hh}$ and $\Delta\nu_3^{hh}$ are indicated as a ratio to $\Delta\nu_1^{hh}$ (d).

ture-independent (Appendix Tables H1–H4). The main peak is positioned at 3445 cm^{-1} ($\Delta\nu_1^{g}$). Two contributions are located at the left shoulder of the broad spectrum, *i.e.,* 3178 ($\Delta\nu_2^{g}$) and 3120 cm^{-1} ($\Delta\nu_3^{g}$). A weak shoulder is present at 3515 cm^{-1} ($\Delta\nu_4^{g}$). The fifth contributions has a peak at 3350 cm^{-1} ($\Delta\nu_5^{g}$) with a broad half-width value and a relatively high intensity. Only a minor change in half-width values is observed between –190° and –120°C, whereas peak positions remain nearly constant (Appendix Tables H1–H4).

EUTECTIC MELTING IN SYNTHETIC FLUID INCLUSIONS

In the previous section, I have shown how Raman spectrometry allows one to detect and distinguish several types of aqueous liquid solutions, ice, salt hydrates and "glasses" in fluid inclusions at low temperatures. Eutectic and peritectic temperatures are, by definition, related to disappearance and appearance of certain phases. For example, at the eutectic temperature in the system H_2O–NaCl, either hydrohalite or ice melts completely, and an aqueous liquid solution appears. Measurement of eutectic and peritectic temperatures in fluid inclusions using solely microthermometry is extremely difficult, as these phase changes are difficult to observe. In small inclusions, even the temperature of final melting of certain phases may be difficult to obtain. In many cases, the recrystallization of glass-like substances is mistaken for a eutectic reaction (Samson & Walker 2000). The combination of Raman spectrometry and

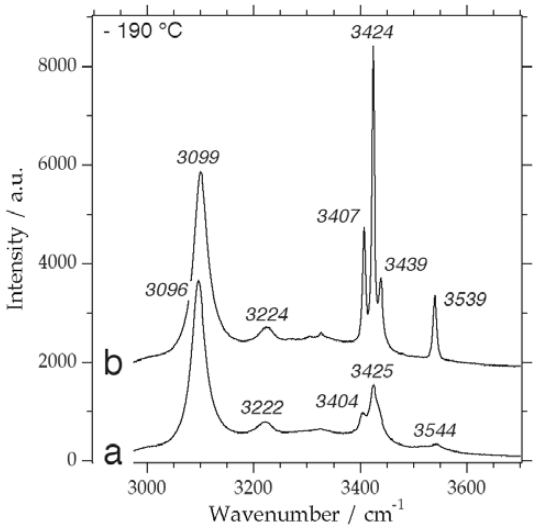

FIG. 12. Comparison of Raman spectra of a NaCl-rich glass (a) and a microcrystalline mixture of ice and hydrohalite (b) at –190°C.

TABLE 1. COMPARISON OF PEAK VALUES AT –170°C FOR ICE, HYDROHALITE AND $MgCl_2$ HYDRATE

	this study	Dubessy *et al.* (1982)	Franks[a]
Ice (Ih)	3105	3090	3095[a]
	3228	3250	
$NaCl•2H_2O$	–	3089	–
	–	3209	–
	3326	–	–
	3407	3406	3413[b]
	3424	3422	3423[b]
	3438	3438	3433[b]
	3540	3536	3531[b]
$MgCl_2•12H_2O$	–	3091	
	–	3110	
	3202	–	
	3322	3328	
	3405	3401	
	3438	3426	
	3465	3462	
	3482	3483	
	3516	3511	

[a] extracted from *Water, a Comprehensive Treatise* (F. Franks, ed.); [a]: Sceats & Rice (1982); [b]: Falk & Knop (1973).

microthermometry can lead to the exact detection of these temperatures, as the spectra are completely different on either side, corresponding to different ice-like or aqueous-liquid-like phases.

Raman spectra of a synthetic NaCl–H_2O fluid inclusion with a 23.2 mass % NaCl composition were taken in a temperature range between –30° and –20°C, at intervals of 1°C (Fig. 24). Near the temperature of final melting of ice at the eutectic point, the interval was decreased to 0.1°C. At –21.2°C, the eutectic point in the relevant system, the Raman spectra change drastically, as a combined ice+hydrohalite signal changes to a combined water+hydrohalite signal. This temperature corresponds exactly to the eutectic temperature given in literature (*e.g.,* Bodnar 1993). Therefore, one can conclude that the laser beam did not warm the inclusion during measurements, and the temperature control by the Linkam stage was not affected.

For a synthetic H_2O–$MgCl_2$ fluid inclusion with a 20.2 mass % $MgCl_2$ composition, a similar procedure of heating was performed in the temperature range between –40° and –30°C. Figure 25 illustrates the development of the Raman signal of a single fluid inclusion during heating in this temperature range. At –34°C, the spectrum consists of two components, *i.e.,* an ice signal and a $MgCl_2•12H_2O$ signal. A temperature of –33.1°C was obtained for the eutectic point from the changing Raman spectra, which corresponds exactly to the value given in literature (*e.g.,* Spencer *et al.* 1990). At –33°C, the remaining spectrum consists of an ice and a brine component. Above the temperature of final melting of ice, –29.2°C, only a brine spectrum is obtained from the fluid inclusion.

DISCUSSION

As Raman spectra directly reflect the nature of bonding within of the analyzed material, the curves obtained may be used to interpret the structure and dynamics of water, brine, ice, glass and salt hydrates. The spectra of brine and water are highly variable with temperature; consequently, the structure of these liquid phases vary strongly. Several models were proposed to qualify this phenomenon (*e.g.,* Stanley & Teixeira 1980, Walrafen *et al.* 1986). The technique applied in this study, *i.e.,* using synthetic fluid inclusions with a maximum diameter of 20 μm, allows the analysis of these phases within metastable conditions. The behavior of water was investigated down to –40°C, NaCl brines down to –90°C, and $MgCl_2$ brines were analyzed down to –190°C. The behavior of the Raman spectra with temperature illustrates the existence of a singular temperature around –35°C, *i.e.,* the temperature at which there are anomalous changes in the properties of water. A similar behavior has been reported by Angell *et al.* (1973) and Hare & Sorensen (1986, 1987) from calorimetry and density measurements, respectively. They interpreted a singularity between –40°C and –45°C in supercooled water. In this study, a NaCl brine could be cooled down to about –85°C, well below its singular temperature around –35°C. In a $MgCl_2$ brine, the singularity occurs at slightly higher temperatures, around –30°C. This comparison illustrates that the temperature of the singularity, or the fundamental change in the structure of water, increases in solutions with higher ionic strength.

A comparison of peak positions of ice, hydrohalite and $MgCl_2•12H_2O$ with values given by Dubessy *et al.* (1982), Sceats & Rice (1982) and Falk & Knop (1973)

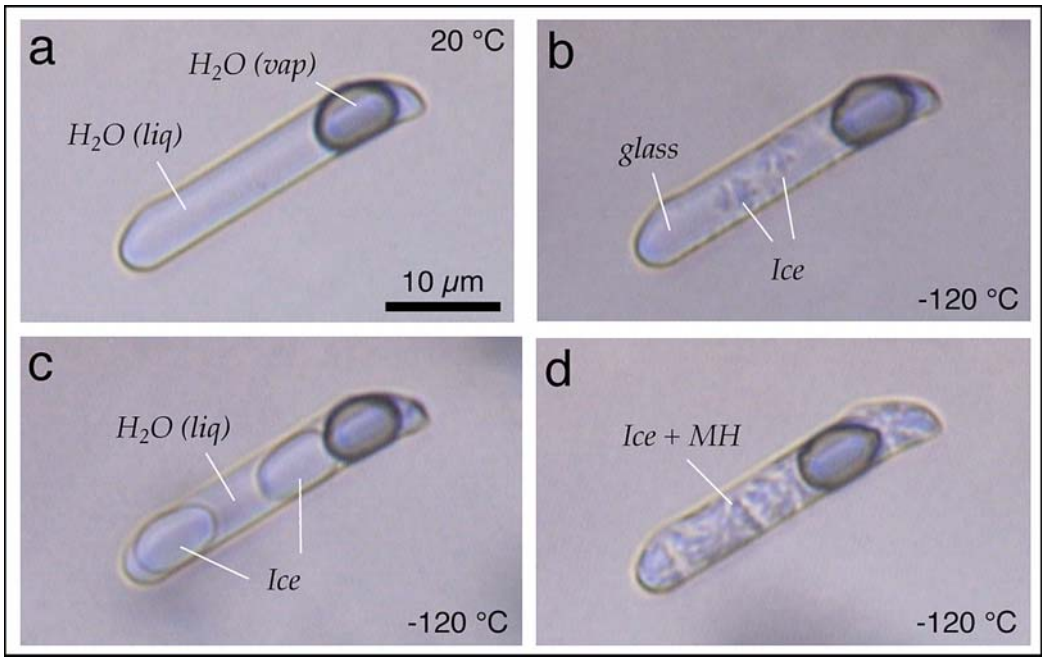

FIG. 13. A synthetic fluid inclusion with a 20.2 mass % $MgCl_2$ solution at selected temperatures: 20°C (a), and –120°C (b, c, and d). See text for further details.

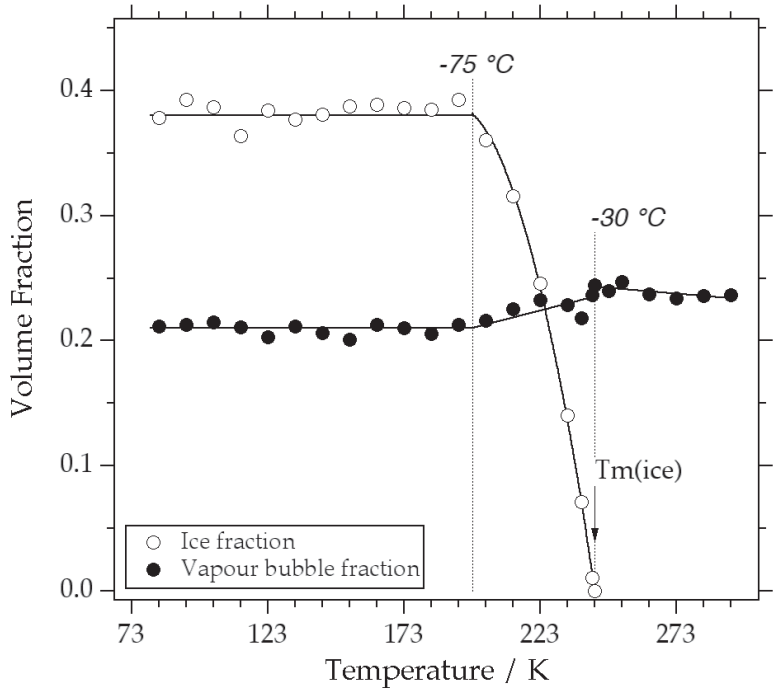

FIG. 14. Volume-fraction estimate of the vapor bubble (solid circles) and ice (open circles) as a function of temperature in the fluid inclusion illustrated in Figure 13c. Volume fractions are obtained from an area analysis of a two-dimensional projection.

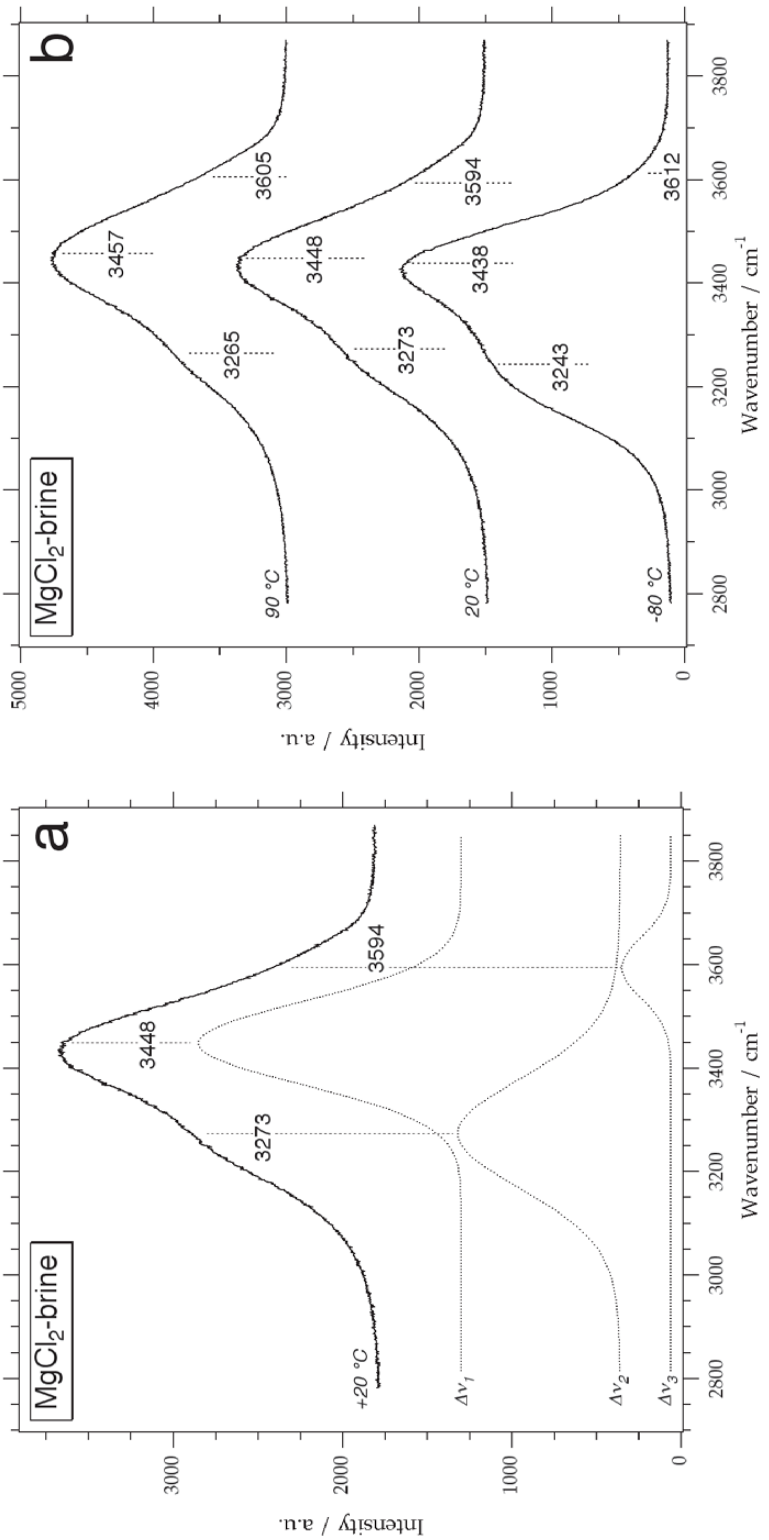

FIG. 15. (a) Raman spectrum of a $MgCl_2$ brine at 20°C with three Gaussian–Lorentzian contributions, $\Delta\nu_1^{aq}$, $\Delta\nu_2^{aq}$ and $\Delta\nu_3^{aq}$. (b) Raman spectra of the brine at +90°, +20° and –80°C, illustrating the shift of Gaussian–Lorentzian contributions with temperature.

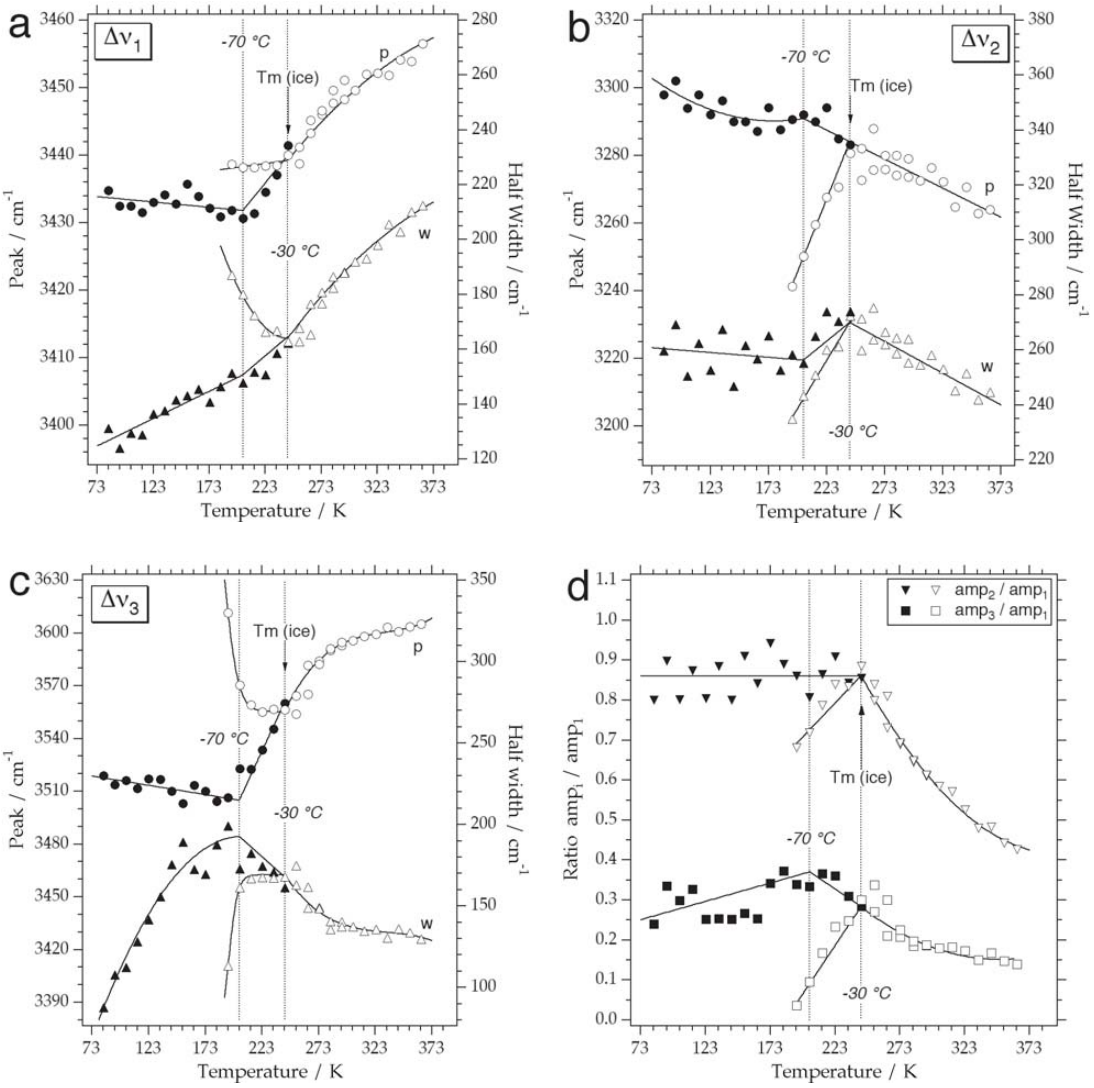

FIG. 16. Temperature dependence of peak position (open and solid circles) and half-width (open and solid triangles) of $\Delta\nu_1^{aq}$ (a), $\Delta\nu_2^{aq}$ (b) and $\Delta\nu_3^{aq}$ (c) of a $MgCl_2$ brine. The open symbols illustrate a brine in the presence of a vapor bubble (as in Fig. 13a), whereas the closed symbols represent a brine in the presence of both a vapor bubble and ice (as in Fig. 13c). The relative intensities of $\Delta\nu_2^{aq}$ and $\Delta\nu_3^{aq}$ are indicated as a ratio to $\Delta\nu_1^{aq}$ (d).

is indicated in Table 1. The main peak of pure ice has a higher wavenumber than indicated by Dubessy *et al.* (1982), whereas the second peak of ice is positioned at much lower values. This large difference is caused by the difference in analytical technique applied to the spectra. In this study, peak values are obtained from the Gaussian–Lorentzian components. Dubessy *et al.* (1982) omitted this fitting procedure and analyzed the peak position straight from the raw spectrum. Consequently, half-width values of specific peaks were not determined. The second peak of ice has a broad half-width value and is not very pronounced; as a result, an estimate of exact position from the raw spectrum is not reliable. The four peaks of hydrohalite are similar in both studies. However, the relative intensities of individual peaks are different. The spectrum given in Dubessy *et al.* (1982) corresponds to a single crystal of hydrohalite with a specific orientation. In this study, I

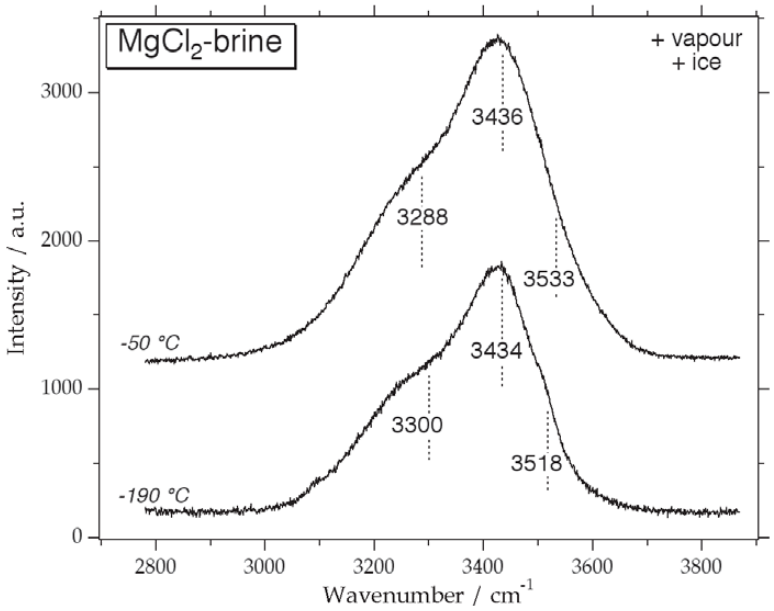

FIG. 17. Comparison of Raman spectra of a $MgCl_2$ brine in the presence of vapor bubble and ice at –190° and –50°C with three Gaussian–Lorentzian contributions, $\Delta\nu_1^{aq}$, $\Delta\nu_2^{aq}$ and $\Delta\nu_3^{aq}$.

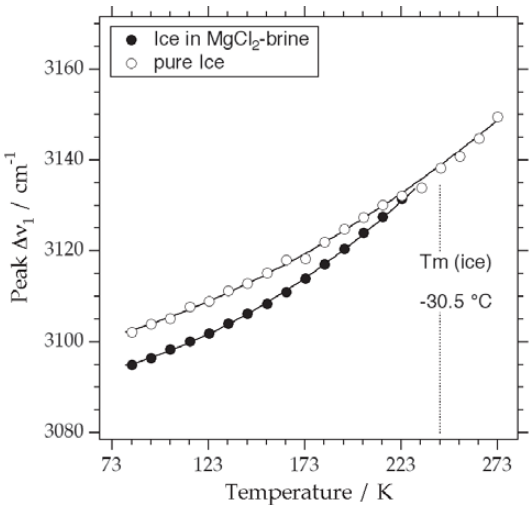

FIG. 18. Difference in peak position of $\Delta\nu_1$ of ice in a $MgCl_2$ brine (solid circles) and pure ice (open circles).

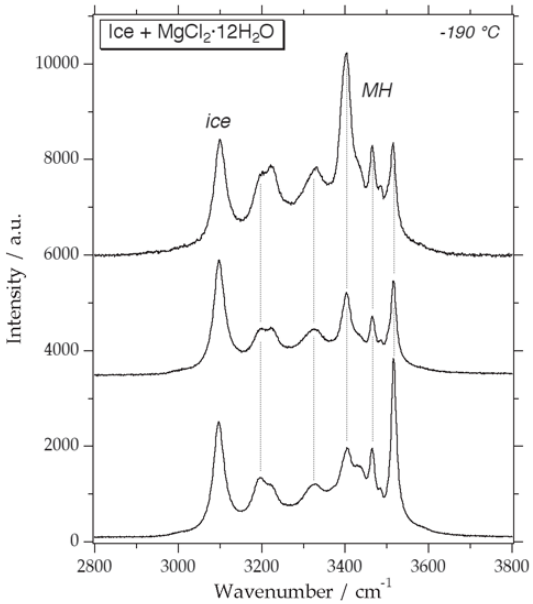

FIG. 19. Variable relative intensities of the Raman peaks belonging to $MgCl_2 \cdot 12H_2O$ (MH) at –190°C, as a consequence of different orientations of the crystals.

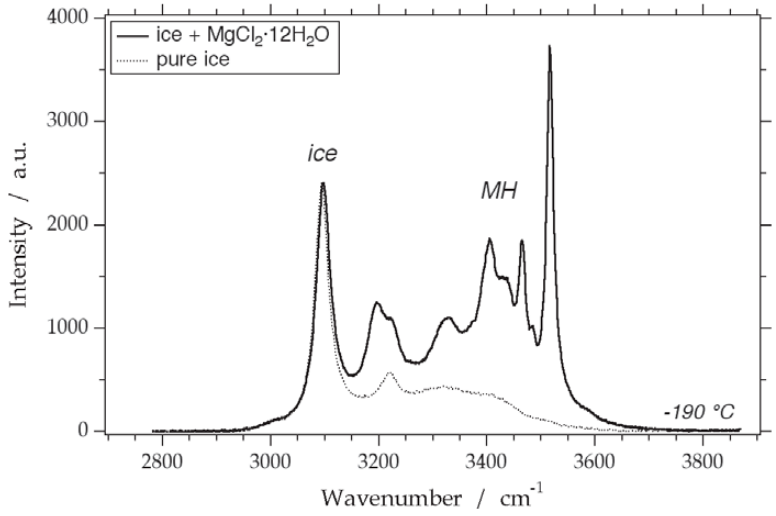

FIG. 20. Raman spectrum of a frozen synthetic fluid inclusions at –190°C with a combination of ice and $MgCl_2$•$12H_2O$ peaks (MH). The dotted curve is a Raman spectrum of pure ice, which is subtracted to obtain a signal purely resulting from $MgCl_2$•$12H_2O$.

showed that fluid inclusions invariably form a microcrystalline mixture with a constant distribution of peaks, *i.e.,* position, half-width and intensity. The low-intensity peak at 3326 cm^{-1} was not recognized by Dubessy *et al.* (1982), and they illustrated two more peaks at 3089 and 3209 cm^{-1}, which probably belong to ice. Dubessy *et al.* (1982) argued that there is no interference between the spectra of ice and those of the hydrates. However, Figures 9 and 20 clearly indicate an overlap of the two spectra. Moreover, the $MgCl_2$•$12H_2O$ has a major Gaussian–Lorentzian contribution (3196 cm^{-1}) that nearly coincides with the second peak of ice. This peak was not identified by Dubessy *et al.* (1982), who illustrated the presence of two other peaks in this region (Table 1), probably belonging to ice.

Temperature control during freezing experiments is of major importance for the cultivation of salt hydrates. For example, $MgCl_2$•$12H_2O$ could only be made to crystallize during slow cooling. Rapid cooling has been recommended in literature on different types of heating–freezing stages (*e.g.,* Roedder 1984). In this study, I show that the crystallization of some salt hydrates is inhibited by rapid cooling, and measurements could only be performed in a metastable system containing a supersaturated brine and ice. The melting temperature of ice obtained is meaningless in terms of total salinity of the aqueous solution. Figure 26 illustrates the occurrence of phase assemblages in three individual fluid inclusions with the aqueous solutions previously described (see also Figs. 6, 13); it summarizes the results of the combined technique of Raman spectroscopy and microthermometry. The temperature overlap of different phase-assemblages, especially in the H_2O–NaCl and H_2O–$MgCl_2$ systems, illustrates the difficulties encountered in interpreting phase changes solely based on microthermometry.

Natural samples from dolomitized carbonic rock in the Upper Muschelkalk (upper Rhein Graben, southwestern Germany) were used to test the method. Small primary fluid inclusions were identified in saddle dolomite (Fig. 27). The inclusions have regular negative crystal shapes, and are in general smaller than 2 μm in diameter. Only a few of them reach a size of about 10 μm. They contain a homogeneous aqueous fluid with about 4 vol.% vapor bubble at room temperature. Total homogenization occurs in the range of 72.5° to 123°C, to the liquid phase. Low-temperature behavior was difficult to observe, and could only be deduced from cycling experiments and Raman spectroscopy. During fast cooling, the vapor bubble increased in size up to 10 vol.% at –100°C. During subsequently heating, the presence of a glass became obvious from recrystallization phenomena, *i.e.,* the vapor bubble disappeared slowly. Around –50°C, the clear glass developed a granular texture in the absence of a vapor bubble. At slightly higher temperatures, the vapor bubble reappeared and floated in a clear mass, in which ice or hydrate crystals were not distinguishable. At approximately –21°C, the vapor bubble moved suddenly to another corner of the inclusion. Finally, around +5°C, the vapor bubble moved again to another corner. Only Raman spectroscopy could reveal the physical meaning of these observations. The fluid inclusion contains a mixture of ice and hydrohalite at –138°C (Fig. 28a).

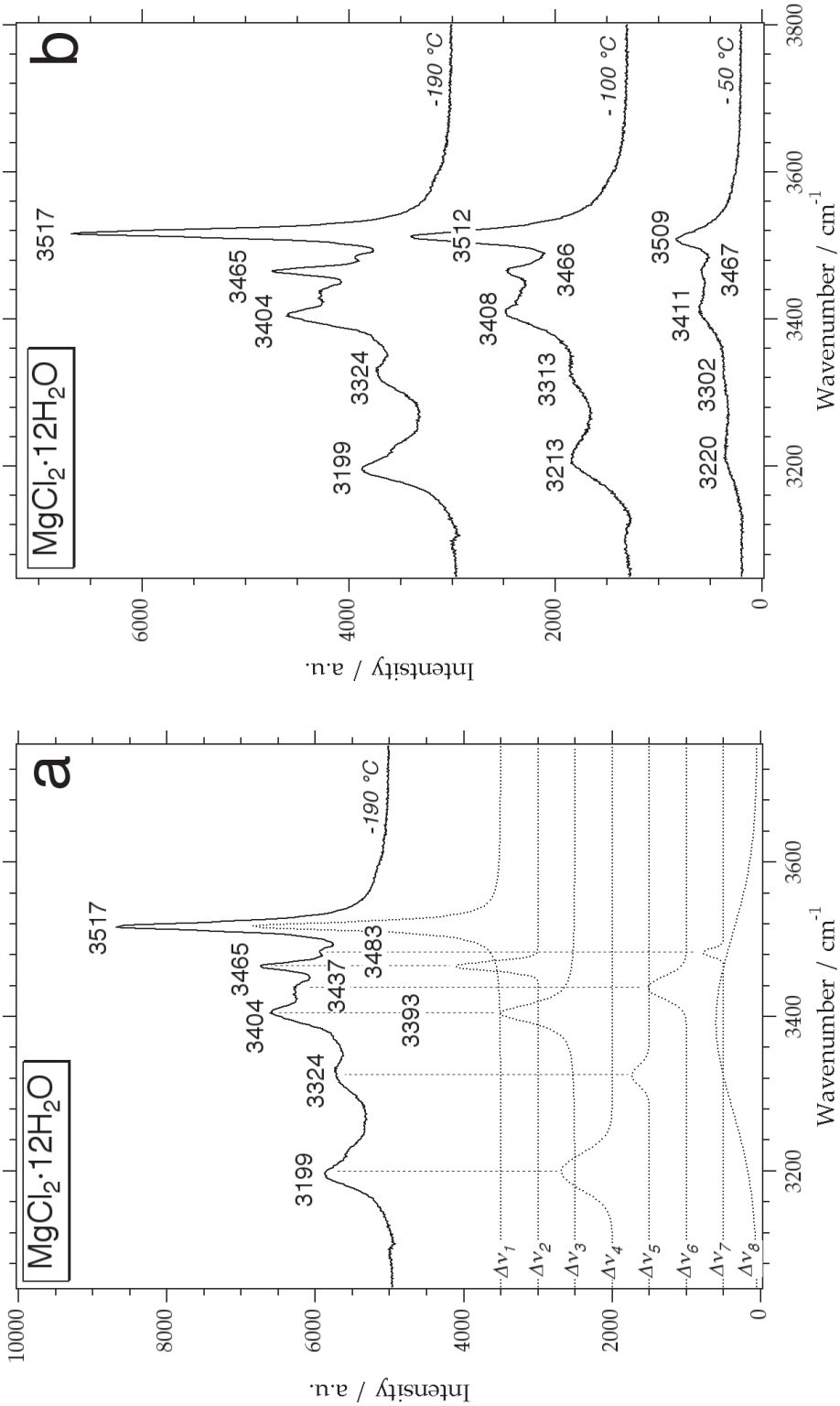

FIG. 21. (a) Raman spectrum of $MgCl_2 \cdot 12H_2O$ at –190°C with eight Gaussian–Lorentzian contributions, $\Delta\nu_1^{mh}$, $\Delta\nu_2^{mh}$, $\Delta\nu_3^{mh}$, $\Delta\nu_4^{mh}$, $\Delta\nu_5^{mh}$, $\Delta\nu_6^{mh}$, $\Delta\nu_7^{mh}$ and $\Delta\nu_8^{mh}$. (b) Raman spectra of $MgCl_2 \cdot 12H_2O$ at –190°, –100° and –50°C, illustrating the shift of Gaussian–Lorentzian contributions with temperature.

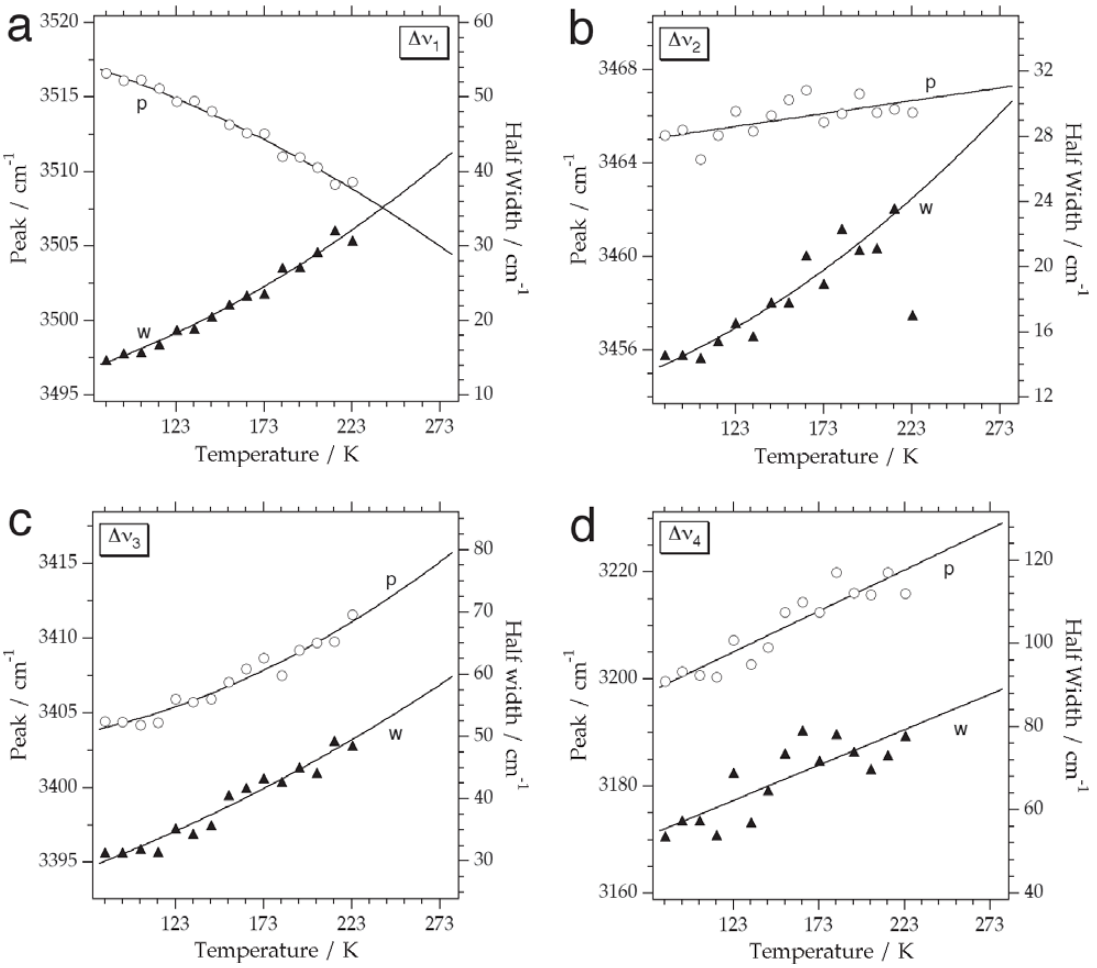

FIG. 22. Temperature dependence of the four main peak positions (open circles) and associated half-width (solid triangles, of $\Delta\nu_1^{mh}$ (a), $\Delta\nu_2^{mh}$ (b), $\Delta\nu_3^{mh}$ (c) and $\Delta\nu_4^{mh}$ (d) of $MgCl_2 \cdot 12H_2O$. The letters p and w indicate the best-fit curves for peak position and half width, respectively.

During the development of the granular texture, the inclusion still contains both solid phases (Fig. 28b). Consequently, this coarsening process does not correspond to eutectic or peritectic melting. The temperature of final melting of ice was estimated at –23.4°C by measuring changes in Raman spectra during stepwise heating. This temperature corresponds approximately to the first sudden movement of the vapor bubble. Subsequently, the inclusion contains an aqueous solution and hydrohalite (Fig. 28c), which finally melts metastably at +4.6°C. Therefore, Raman spectroscopy has revealed true melting temperatures of the phases present at low temperatures in the fluid inclusion, and it has revealed the nature of the type of dissolved salt, *i.e.,* NaCl. Furthermore, the temperature of ice melting indicates the presence of another type of salt, as it is below the eutectic temperature of the binary system H_2O–NaCl. The positive temperature of melting of hydrohalite in the presence of a vapor bubble could have been mistaken for clathrate melting. However, Raman spectroscopy clearly indicates the presence of hydrohalite, and gases like CO_2 or CH_4 could not be detected in the vapor bubble.

CONCLUSIONS

A combined Gaussian–Lorentzian fitting procedure allows an exact reproduction of the measured Raman spectra of aqueous solutions. The spectrum of water consists of three deconvoluted bands, that of ice and

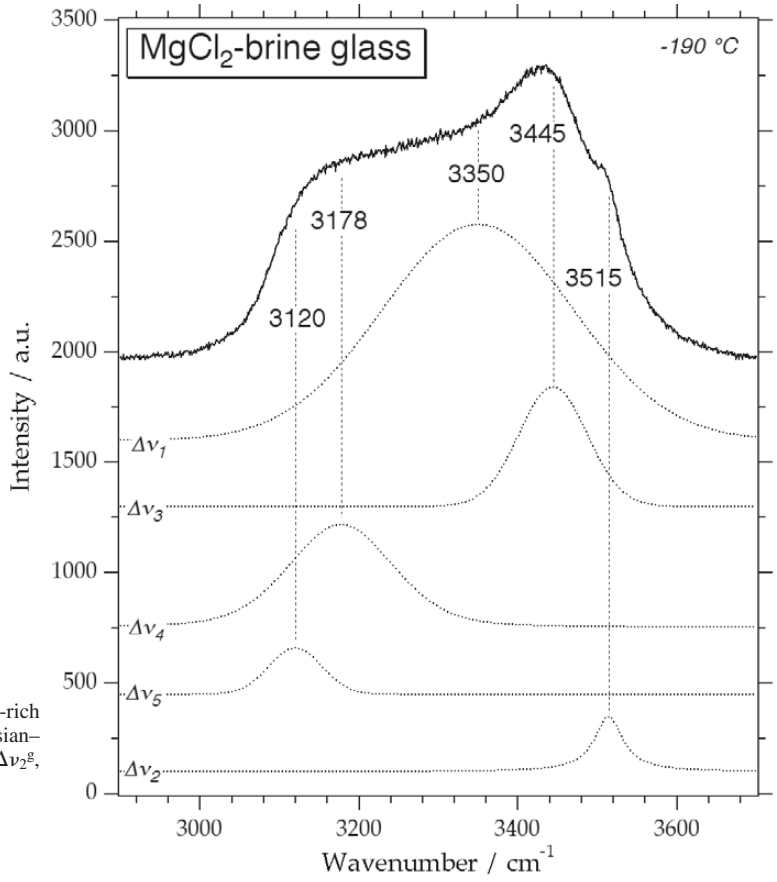

FIG. 23. Raman spectrum of $MgCl_2$-rich glass at –190°C with five Gaussian–Lorentzian contributions, $\Delta\nu_1^g$, $\Delta\nu_2^g$, $\Delta\nu_3^g$, $\Delta\nu_4^g$ and $\Delta\nu_5^g$.

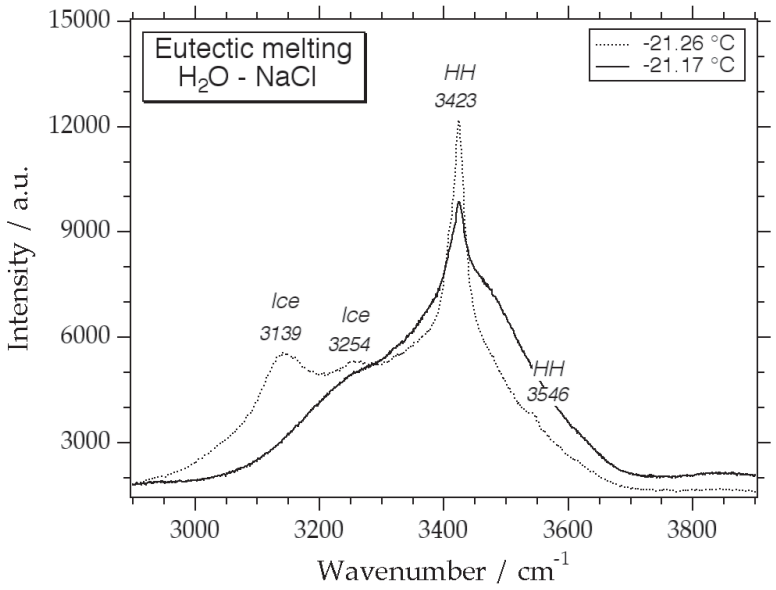

FIG. 24. Raman spectra of a synthetic fluid inclusion with a 23.2 mass % NaCl solution at either side of the eutectic temperature. HH: hydrohalite. The heating–freezing stage was calibrated directly after measurements, resulting in a correction with a two-decimal indication of temperature.

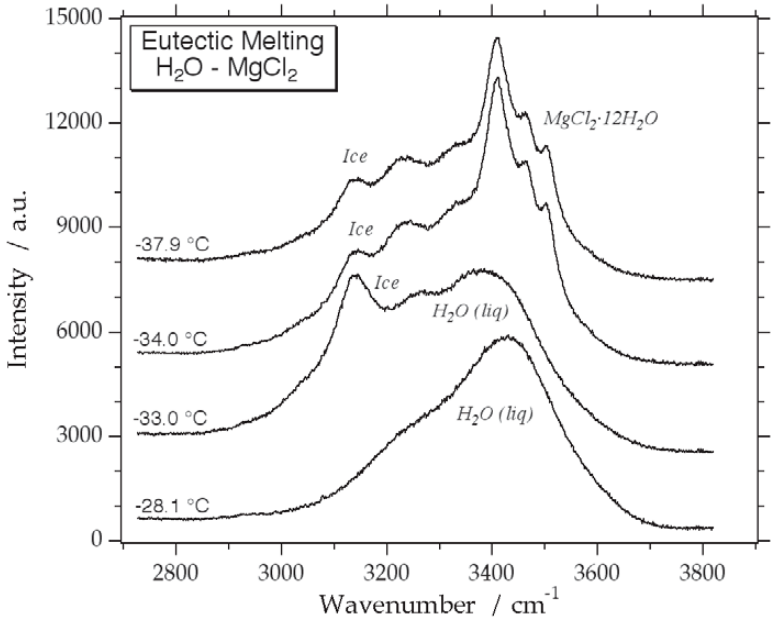

FIG. 25. Series of Raman spectra of a synthetic fluid inclusion with a 20.2 mass % $MgCl_2$ solution between –37.9° and –28.1°C, reflecting eutectic melting (at –33.1°C) and final melting of ice (at –28.2°C).

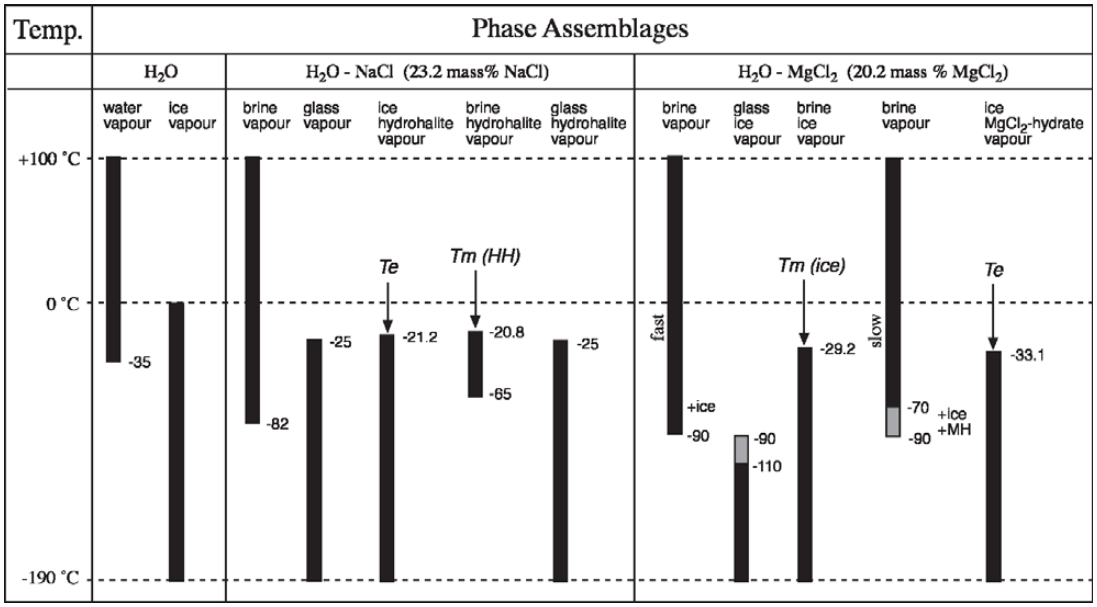

FIG. 26. Phase assemblages as a function of temperature (Temp.) in three fluid inclusions with a pure H_2O, H_2O–NaCl and H_2O–$MgCl_2$ fluid. Numbers are in °C, corresponding to phase changes described in the section "Results"; fast and slow refer to fast (40°/min) and slow (5°/min) cooling runs, respectively. Te and Tm are the eutectic and final melting temperature, respectively. HH and MH are hydrohalite and $MgCl_2$ hydrate, respectively.

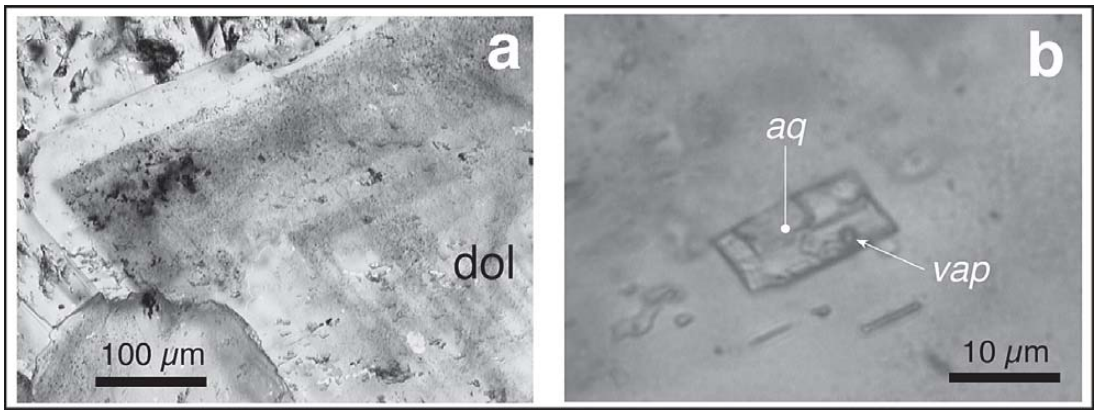

FIG. 27. (a) Zoned crystal of dolomite from a drill core of Muschelkalk (Triassic) in the upper Rhein graben (Rot, Germany). The dolomite reveals a high concentration of tiny inclusions (shading of crystal). (b) Fluid inclusion with regular shape, containing a saline aqueous liquid solution (aq) and a vapor bubble (vap).

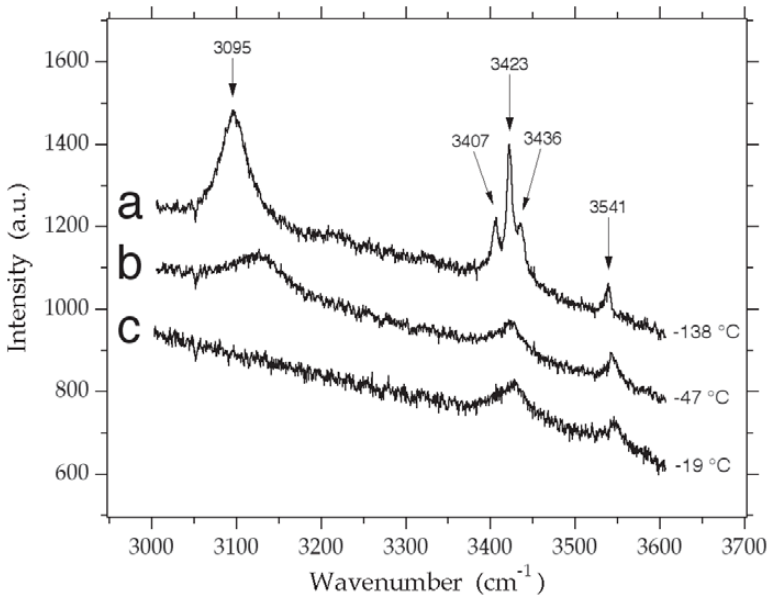

FIG. 28. Series of Raman spectra of a natural fluid inclusion in dolomite (see Fig. 26) at –138°C (a), –47°C (b), and –19°C (a), indicating the presence of ice and hydrohalite.

hydrohalite, six bands, that of $MgCl_2 \cdot 12H_2O$, eight bands. Both hydrohalite and $MgCl_2 \cdot 12H_2O$ have well-defined narrow peaks. The Raman spectrum of $MgCl_2$–H_2O "glass" resembles that of a brine, but consists of five deconvoluted bands and is much broader. The NaCl–H_2O "glass" resembles that of a combination of ice and hydrohalite at much lower intensities and greater half-widths.

A brine spectrum is substantially different from the spectrum of pure water. The relative peak position, half-width and intensity of the three Gaussian–Lorentzian bands are affected by both temperature and salinity.

The deconvoluted Gaussian–Lorentzian bands of ice are affected by the presence of a brine and salt hydrate. The main peak of each is shifted by 5 and 10 cm^{-1}, respectively, to lower wavenumbers.

The distribution and occurrence of ice-like phases, salt hydrates, brine and water in fluid inclusions are highly dependent on the freezing–heating procedure. Up to four different phase-configurations may appear in the same inclusion at the same temperature. The presence of a brine and ice at very low temperatures (–190°C) may regularly occur, and represents a metastable configuration, which cannot be re-equilibrated by recrystallization.

The freezing behavior of a $MgCl_2$ brine and a NaCl brine are substantially different. Rapid cooling causes the formation of a hydrohalite–ice-like glass from NaCl solutions, and a brine-like glass from $MgCl_2$ solutions, in the presence of small crystals of ice. The NaCl glass recrystallizes to a microcrystalline mixture of ice and hydrohalite a few degrees above the eutectic temperature. The $MgCl_2$ brine crystallizes partly to ice and a supersaturated brine around –110°C. A $MgCl_2$ hydrate could not be formed by rapid cooling.

The combination of Raman spectrometry and microthermometry allows an exact estimate of phase changes within fluid inclusions during freezing–heating experiments. Eutectic temperatures in the systems NaCl–H_2O and $MgCl_2$–H_2O were exactly reproduced in fluid inclusions by this combined technique.

A NaCl brine has a singular temperature around –35°C, and a $MgCl_2$ brine has one around –30°C, where the properties of water exhibit an anomalous behavior. This singularity could not be reached for pure water, as the nucleation of ice occurred at slightly higher temperatures, around –40° to –35°C. Those singularities could not be detected from the raw spectra, but were obvious from trends in the Gaussian–Lorentzian components.

Measurements of melting temperatures of ice-like materials within fluid inclusions containing a metastable phase-assemblage may result in erroneous estimations of salinity.

Acknowledgements

D.J. Kontak, R.F. Martin, T.P. Mernagh, and R. Moritz are thanked for their critical reviews of the manuscript.

References

Angell, C.A., Shuppert, J. & Tucker J.C. (1973): Anomalous properties of supercooled water, heat capacity, expansivity, and proton magnetic resonance chemical shift from 0 to –38°C. *J. Phys. Chem.* **77**, 3092-3099.

Bakker, R.J. (2001): Combined Raman spectroscopy and low temperature microthermometry. *In* XVI European Current Research on Fluid Inclusions (F. Noronha, A. Dória & A. Guedes, eds.). *Faculdade de Ciências do Porto, Departamento de Geologia, Memória* **7**, 15-18.

_____ (2002): Identification of salts in fluid inclusions by combined Raman spectroscopy and low temperature microthermometry. *In* Eighth Biennial Pan-American Conference on Research on Fluid Inclusions, Program with Abstracts (D.J. Kontak & A.J. Anderson, eds.). Nova Scotia Department of Natural Resources and the Queen's Printer (3-6).

Bodnar, R.J. (1993): Revised equation and table for determining the freezing point depression of H_2O–NaCl solutions. *Geochim. Cosmochim. Acta* **57**, 683-684.

_____ & Sterner, S.M. (1987): Synthetic fluid inclusions. *In* Hydrothermal Experimental Techniques (G.C. Ulmer & H.L. Barnes, eds.). John Wiley & Sons, New York, N.Y. (423-457).

Burke, E.A.J. (2001): Raman microspectrometry of fluid inclusions. *Lithos* **55**, 139-158.

Dubessy, J., Audeoud, D., Wilkins, R. & Kosztolanyi, C. (1982): The use of the Raman microprobe Mole in the determination of the electrolytes dissolved in the aqueous phase of fluid inclusions. *Chem. Geol.* **37**, 137-150.

_____, Larghi, L. & Canals, M. (1997): Reconstruction of ionic composition of fluid inclusions. *In* Proc. XIVth European Current Research on Fluid Inclusions, Nancy (M.C. Boiron & J. Pironon, eds.). CNRS–CREGU, Nancy, France (90-91).

Falk, M. & Knop, O. (1973): Water in stoichiometric hydrates. *In* Water, a Comprehensive Treatise. **2**. Water in Crystalline Hydrates, Aqueous Solutions of Simple Nonelectrolytes (F. Franks, ed.). Plenum Press, New York, N.Y. (55-113).

Franks, F. (1973): *Water, a Comprehensive Treatise*. **2**. *Water in Crystalline Hydrates, Aqueous Solutions of Simple Nonelectrolytes.* **3**. *Aqueous Solutions of Simple Electrolytes*. Plenum Press, New York, N.Y.

Frantz, J.D., Dubessy, J. & Mysen, B. (1993): An optical cell for Raman spectroscopic studies of supercritical fluids and its application to the study of water to 500°C and 2000 bar. *Chem. Geol.* **106**, 9-26.

Goldstein, R.H. & Reynolds, T.J. (1994): Systematics of fluid inclusions in diagenetic minerals. *Soc. Econ. Paleontol. Mineral., Short Course* **31**.

Hare, D.E. & Sorensen C.M. (1986): Densities of supercooled H_2O and D_2O in 25 μm glass capillaries. *J. Chem. Phys.* **84**, 5085-5089.

_____ & _____ (1987): The density of supercooled water. II. Bulk samples cooled to the homogeneous nucleation limit. *J. Chem. Phys.* **87**, 4840-4845.

LILLEY, T.H. (1973): Raman spectroscopy of aqueous electrolyte solutions. *In* Water, a Comprehensive Treatise. **3**. Aqueous Solutions of Simple Electrolytes (F. Franks, ed.). Plenum Press, New York, N.Y. (265-300).

MERNAGH, T.P. & WILDE, A.R. (1989): The use of the laser Raman microprobe for the determination of salinity in fluid inclusions. *Geochim. Cosmochim. Acta* **53**, 765-771.

ROEDDER, E. (1984): Fluid inclusions. *Rev. Mineral.* **12**.

SAMSON, I.M. & WALKER R.T. (2000): Cryogenic Raman spectroscopic studies in the system NaCl–$CaCl_2$–H_2O and implications for low-temperature phase behavior in aqueous fluid inclusions. *Can. Mineral.* **38**, 35-43.

SCEATS, M.G. & RICE, S.A. (1982): Amorphous solid water and its relationship to liquid water: a random network model for water. *In* Water, a Comprehensive Treatise. **7**. Water and Aqueous Solutions at Subzero Temperatures (F. Franks, ed.). Plenum Press, New York, N.Y. (83-214).

SPENCER, R.J., MØLLER, N. & WEARE, J.H. (1990): The prediction of mineral solubilities in natural waters: a chemical equilibrium model for the Na–K–Ca–Mg–Cl–SO_4–H_2O system at temperatures below 25°C. *Geochim. Cosmochim. Acta* **54**, 575-590.

STANLEY, H.E. & TEIXEIRA, J. (1980): Interpretation of the unusual behavior of H_2O and D_2O at low temperatures: test of a percolation model. *J. Chem. Phys.* **73**, 3404-3422.

ULNESS, D.J., KIRKWOOD, J.C. & ALBRECHT, A.C. (2001): Raman spectroscopy. *In* Encyclopedia of Chemical Physics and Physical Chemistry. II. Methods, Part B1 (J.H. Moore & N.D. Spencer, eds.). Institute of Physics Publishing, Bristol, U.K. (1017-1062).

WALRAFEN G.E. (1972): Raman and infrared spectral investigations of water structure. *In* Water, a Comprehensive Treatise. **1**. The Physics and Physical Chemistry of Water (F. Franks, ed.). Plenum Press, New York, N.Y. (151-214).

_____, FISHER, M.R., HOKMABADI, M.S. & YANG, W.A. (1986): Temperature dependence of the low- and high-frequency Raman scattering from liquid water. *J. Chem. Phys.* **85**, 6970-6982.

Received November 15, 2002, revised manuscript accepted August 24, 2003.

APPENDICES

Peak positions, half-width values, amplitude ratios and Gauss factors are fitted to a polynomial equation in temperature (eq. A1), a sigmoid function (eq. A2), or a Lorentz function (eq. A3). The parameters of the fitting curves are given in the following tables.

$$f(x) = a_0 + a_1T + a_2T^2 + a_3T^3 \quad \text{(A1)}$$

$$f(x) = b_0 + \frac{b_1}{1 + \exp\left(\frac{b_2 - T}{b_3}\right)} \quad \text{(A2)}$$

$$f(x) = c_0 + \frac{c_1}{(T - c_2)^2 + c_3} \quad \text{(A3)}$$

Appendix A. Water

TABLE A1. PARAMETERS IN EQUATION A1 TO CALCULATE PEAK VALUES OF WATER

	a_0	a_1	a_2	a_3
$\Delta\nu_1$	2432.3	8.1038	−0.021876	$2.0041\cdot10^{-5}$
$\Delta\nu_2$	2280.6	7.4925	−0.019838	$1.7856\cdot10^{-5}$
$\Delta\nu_3$	3696.3	−0.7151	0.0024723	$-3.2519\cdot10^{-6}$

TABLE A2. PARAMETERS IN EQUATION A1 TO CALCULATE HALF-WIDTH VALUES OF WATER

	a_0	a_1	a_2	a_3
$\Delta\nu_1$	280.9	−0.10896	–	–
$\Delta\nu_2$	−1020.7	10.962	−0.031448	$2.9345\cdot10^{-5}$
$\Delta\nu_3$	26.865	0.28989	–	–

TABLE A3. PARAMETERS IN EQUATION A1 TO CALCULATE AMPLITUDE RATIOS OF WATER

	a_0	a_1	a_2
$\Delta\nu_2/\Delta\nu_1$	3.2346	−0.011052	$1.0011\cdot10^{-5}$
$\Delta\nu_3/\Delta\nu_1$	−0.38557	0.0026312	$-2.7249\cdot10^{-6}$

TABLE A4. PARAMETERS IN EQUATION A1 TO CALCULATE GAUSS FRACTION VALUES OF WATER

	a_0	a_1
$\Delta\nu_1$	1	–
$\Delta\nu_2$	0.76741	−0.00087464
$\Delta\nu_3$	1	–

Appendix B. Ice

TABLE B1. PARAMETERS IN EQUATION A1 TO CALCULATE PEAK VALUES OF ICE

	a_0	a_1	a_2
$\Delta\nu_1$	3094.3	0.05498	0.00051841
$\Delta\nu_2$	3214.0	0.11898	0.00018459
$\Delta\nu_3$	2990.6	0.14529	0.00028922
$\Delta\nu_4$	3338.3	−0.070014	0.00076117
$\Delta\nu_5$	3405.1	0.11277	–
$\Delta\nu_6$	3236.8	0.21505	–

TABLE B2. PARAMETERS IN EQUATION A1 TO CALCULATE HALF-WIDTH VALUES OF ICE

	a_0	a_1	a_2	a_3
$\Delta\nu_1$	40.207	−0.39376	0.0041831	$7.1178\cdot10^{-6}$
$\Delta\nu_2$	13.355	0.18873	–	–
$\Delta\nu_3$	−16.56	0.53843	–	–
$\Delta\nu_4$	77.247	–	–	–
$\Delta\nu_5$	66.354	0.026498	–	–
$\Delta\nu_6$	308.24	0.052989	–	–

TABLE B3. PARAMETERS IN EQUATION A1 TO CALCULATE AMPLITUDE RATIOS OF ICE

	a_0	a_1	a_2	a_3
$\Delta\nu_2/\Delta\nu_1$	0.067253	–	–	–
$\Delta\nu_3/\Delta\nu_1$	0.017219	−0.00053452	$5.5643\cdot10^{-6}$	–
$\Delta\nu_4/\Delta\nu_1$	0.0085562	0.00031735	–	–
$\Delta\nu_5/\Delta\nu_1$	0.009864	0.00029357	–	–
$\Delta\nu_6/\Delta\nu_1$	0.22483	−0.0016911	$7.6874\cdot10^{-6}$	$1.8942\cdot10^{-8}$

TABLE B4. PARAMETERS IN EQUATION A2 TO CALCULATE GAUSS FRACTION VALUES OF ICE

	b_0	b_1	b_2	b_3
$\Delta\nu_1$	0.0	1.39634	299.499	15.4955
$\Delta\nu_2$	1.0	−1.0	141.179	8.90742
$\Delta\nu_3$	1.0	−1.0	160.543	5.01269
$\Delta\nu_4$	1.0	–	–	–
$\Delta\nu_5$	1.0	–	–	–
$\Delta\nu_6$	0.6882	0.311741	111.446	10.6304

Appendix C. NaCl Brine

TABLE C1a. PARAMETERS IN EQUATION A1 TO CALCULATE PEAK VALUES OF NaCl BRINE BELOW −35°C

	a_0	a_1
$\Delta\nu_1$	3413.4	0.16632
$\Delta\nu_2$	3116.81	0.59295
$\Delta\nu_3$	3718.2	−0.44653

TABLE C1b. PARAMETERS IN EQUATION A1 TO CALCULATE PEAK VALUES OF NaCl BRINE ABOVE −35°C

	a_0	a_1	a_2
$\Delta\nu_1$	3469.3	−0.16834	0.00041968
$\Delta\nu_2$	3191.1	0.43391	−0.00064206
$\Delta\nu_3$	3528.8	0.54531	−0.00082518

TABLE C2a. PARAMETERS IN EQUATION A1 TO CALCULATE HALF-WIDTH VALUES OF NaCl BRINE BELOW −35°C

	a_0	a_1
$\Delta\nu_1$	254.58	−0.23777
$\Delta\nu_2$	154.537	0.32086
$\Delta\nu_3$	−99.96	0.924

TABLE C2b. PARAMETERS IN EQUATION A1 TO CALCULATE HALF-WIDTH VALUES OF NaCl BRINE ABOVE −35°C

	a_0	a_1	a_2
$\Delta\nu_1$	164.34	0.14117	–
$\Delta\nu_2$	271.92	−0.17203	–
$\Delta\nu_3$	342.27	−1.5403	0.0025504

TABLE C3a. PARAMETERS IN EQUATION A1 TO CALCULATE AMPLITUDE RATIOS OF NaCl BRINE BELOW −35°C

	a_0	a_1
$\Delta\nu_2/\Delta\nu_1$	0.71925	−0.00064245
$\Delta\nu_3/\Delta\nu_1$	−0.430861	0.0022377

TABLE C3b. PARAMETERS IN EQUATION A1 TO CALCULATE AMPLITUDE RATIOS OF NaCl BRINE ABOVE −35°C

	a_0	a_1
$\Delta\nu_2/\Delta\nu_1$	1.0557	−0.0020552
$\Delta\nu_3/\Delta\nu_1$	0.78153	$8.4388\cdot10^{-5}$

TABLE C4. PARAMETERS IN EQUATION A2
TO CALCULATE GAUSS FRACTION VALUES OF NaCl BRINE

	b_0	b_1	b_2	b_3
$\Delta\nu_1$	–	1.0	177.696	11.3988
$\Delta\nu_2$	1.0	–0.5	254.716	40.0197
$\Delta\nu_3$	1.0	–0.8	300.411	44.3349

Appendix D. Hydrohalite

TABLE D1a. PARAMETERS IN EQUATION A1
TO CALCULATE PEAK VALUES OF HYDROHALITE

	a_0	a_1	a_2
$\Delta\nu_1$	3424.2	–0.0037114	$4.6925\cdot10^{-5}$
$\Delta\nu_2$	3405.8	0.0083002	$6.0449\cdot10^{-5}$
$\Delta\nu_3$	3440.3	–0.019468	–
$\Delta\nu_4$	3535.4	0.048576	–
$\Delta\nu_5$	3327.1	–0.0045753	–0.00010315

TABLE D1b. PARAMETERS IN EQUATION A3
TO CALCULATE PEAK VALUES OF HYDROHALITE

	c_0	c_1	c_2	c_3
$\Delta\nu_6$	3515.83	–71027.5	187.414	980.865

TABLE D2a. PARAMETERS IN EQUATION A1
TO CALCULATE HALF-WIDTH VALUES OF HYDROHALITE

	a_0	a_1	a_2
$\Delta\nu_1$	–0.33414	0.062874	–
$\Delta\nu_2$	3.9057	–0.0022915	0.00028995

TABLE D2b. PARAMETERS IN EQUATION A2
TO CALCULATE HALF-WIDTH VALUES OF HYDROHALITE

	b_0	b_1	b_2	b_3
$\Delta\nu_3$	7.83758	155.169	354.351	56.9342
$\Delta\nu_4$	7.91738	11.5538	225.127	28.5795

TABLE D2c. PARAMETERS IN EQUATION A3
TO CALCULATE HALF-WIDTH VALUES OF HYDROHALITE

	c_0	c_1	c_2	c_3
$\Delta\nu_5$	9.9826	–	–	–
$\Delta\nu_6$	145.611	239757.0	177.508	2497.65

TABLE D3. PARAMETERS IN EQUATION A1
TO CALCULATE AMPLITUDE RATIOS OF HYDROHALITE

	a_0	a_1	a_2	a_3
$\Delta\nu_2/\Delta\nu_1$	0.3527	0.0018121	$-2.3576\cdot10^{-5}$	$8.0838\cdot10^{-8}$
$\Delta\nu_3/\Delta\nu_1$	–0.25465	0.010539	$-7.5602\cdot10^{-5}$	$1.9298\cdot10^{-7}$
$\Delta\nu_4/\Delta\nu_1$	0.20364	0.00055598	–	–
$\Delta\nu_5/\Delta\nu_1$	0.0094246	$8.0162\cdot10^{-5}$	–	–
$\Delta\nu_6/\Delta\nu_1$	0.0080415	$-7.6362\cdot10^{-5}$	$1.9783\cdot10^{-6}$	–

TABLE D4a. PARAMETERS IN EQUATION A2
TO CALCULATE GAUSS FRACTION VALUES OF HYDROHALITE

	b_0	b_1	b_2	b_3
$\Delta\nu_1$	0.068758	0.503395	208.822	20.0612
$\Delta\nu_2$	0.17239	–	–	–
$\Delta\nu_3$	0.0	–	–	–
$\Delta\nu_4$	1.0	–1.0	86.6571	39.1308
$\Delta\nu_5$	0.0	–	–	–
$\Delta\nu_6$	1.0	–	–	–

APPENDIX E. $MgCl_2$ BRINE (+ VAPOR)

TABLE E1a. PARAMETERS IN EQUATION A1
TO CALCULATE PEAK VALUES OF $MgCl_2$ BRINE BELOW –30°C

	a_0	a_1
$\Delta\nu_1$	3433.7	0.02263
$\Delta\nu_3$	3105.913	0.71103

TABLE E1b. PARAMETERS IN EQUATION A2
TO CALCULATE PEAK VALUES OF $MgCl_2$ BRINE BELOW –30°C

	b_0	b_1	b_2	b_3
$\Delta\nu_3$	3692.744	–137.583	191.0959	$5.3469\cdot10^{-5}$

TABLE E1c. PARAMETERS IN EQUATION A1
TO CALCULATE PEAK VALUES OF $MgCl_2$ BRINE ABOVE –30°C

	a_0	a_1	a_2	a_3
$\Delta\nu_1$	3361.42	0.437114	–0.0004822	–
$\Delta\nu_2$	3305.9	–0.11184	–	–
$\Delta\nu_3$	1625.7	17.691	–0.053123	$5.3469\cdot10^{-5}$

TABLE E2a. PARAMETERS IN EQUATION A1
TO CALCULATE HALF-WIDTH VALUES OF $MgCl_2$ BRINE BELOW –30°C

	a_0	a_1	a_2
$\Delta\nu_1$	697.887	–4.36778	0.0089312
$\Delta\nu_2$	120.524	0.6043	–

TABLE E2b. PARAMETERS IN EQUATION A2
TO CALCULATE HALF-WIDTH VALUES OF $MgCl_2$ BRINE BELOW –30°C

	b_0	b_1	b_2	b_3
$\Delta\nu_3$	69.089	100.0	194.2075	3.75735

TABLE E2c. PARAMETERS IN EQUATION A1
TO CALCULATE HALF-WIDTH VALUES OF $MgCl_2$ BRINE ABOVE –30°C

	a_0	a_1	a_2	a_3
$\Delta\nu_1$	–42.093	1.15	–0.0012455	–
$\Delta\nu_2$	315.97	–0.19949	–	–
$\Delta\nu_3$	1631.0	–13.334	0.039776	$-3.9747\cdot10^{-5}$

TABLE E3a. PARAMETERS IN EQUATION A1
TO CALCULATE AMPLITUDE RATIOS OF $MgCl_2$ BRINE BELOW –30°C

	a_0	a_1
$\Delta\nu_2/\Delta\nu_1$	0.077384	0.0032203
$\Delta\nu_3/\Delta\nu_1$	0.8662656	0.0047656

TABLE E3b. PARAMETERS IN EQUATION A1
TO CALCULATE AMPLITUDE RATIOS OF $MgCl_2$ BRINE ABOVE –30°C

	a_0	a_1	a_2	a_3
$\Delta\nu_2/\Delta\nu_1$	3.4029	–0.015089	$1.9052\cdot10^{-5}$	–
$\Delta\nu_3/\Delta\nu_1$	4.3674	–0.035687	0.0001012	$-9.6049\cdot10^{-8}$

TABLE E4. PARAMETERS IN EQUATION A2
TO CALCULATE GAUSS FRACTION VALUES OF $MgCl_2$ BRINE

	b_0	b_1	b_2	b_3
$\Delta\nu_1$	1.0	–	–	–
$\Delta\nu_2$	1.0	–1.0	369.906	69.082
$\Delta\nu_3$	1.0	–	–	–

APPENDIX F. $MgCl_2$ BRINE (+ VAPOR AND ICE)

TABLE F1a. PARAMETERS IN EQUATION A1
TO CALCULATE PEAK VALUES OF $MgCl_2$ BRINE
IN THE PRESENCE OF ICE AND VAPOR BUBBLE BELOW –70°C

	a_0	a_1	a_2
$\Delta\nu_1$	3435.0	–0.015828	–
$\Delta\nu_2$	3326.5	–0.40882	0.0011503
$\Delta\nu_3$	3526.4	–0.10619	–

TABLE F1b. PARAMETERS IN EQUATION A1
TO CALCULATE PEAK VALUES OF $MgCl_2$ BRINE
IN THE PRESENCE OF ICE AND VAPOR BUBBLE ABOVE –70°C

	a_0	a_1
$\Delta\nu_1$	3390.23	0.20453
$\Delta\nu_2$	3317.679	–0.13172
$\Delta\nu_3$	3222.94	1.3876

TABLE F2a. PARAMETERS IN EQUATION A1
TO CALCULATE HALF-WIDTH VALUES OF $MgCl_2$ BRINE
IN THE PRESENCE OF ICE AND VAPOR BUBBLE BELOW –70°C

	a_0	a_1	a_2
$\Delta\nu_1$	110.23	0.19903	–
$\Delta\nu_2$	263.3	–0.034777	–
$\Delta\nu_3$	–106.48	2.9152	–0.0071036

TABLE F2b. PARAMETERS IN EQUATION A1
TO CALCULATE HALF-WIDTH VALUES OF $MgCl_2$ BRINE
IN THE PRESENCE OF ICE AND VAPOR BUBBLE ABOVE −70°C

	a_0	a_1
$\Delta\nu_1$	101.698	0.24103
$\Delta\nu_2$	170.538	0.42184
$\Delta\nu_3$	318.86	−0.62161

TABLE F3a. PARAMETERS IN EQUATION A1
TO CALCULATE AMPLITUDE RATIOS OF $MgCl_2$ BRINE
IN THE PRESENCE OF ICE AND VAPOR BUBBLE BELOW −70°C

	a_0	a_1
$\Delta\nu_2/\Delta\nu_1$	0.8604	–
$\Delta\nu_3/\Delta\nu_1$	0.1712	0.00095126

TABLE F3b. PARAMETERS IN EQUATION A1
TO CALCULATE AMPLITUDE RATIOS OF $MgCl_2$ BRINE
IN THE PRESENCE OF ICE AND VAPOR BUBBLE ABOVE −70°C

	a_0	a_1
$\Delta\nu_2/\Delta\nu_1$	0.8604	–
$\Delta\nu_3/\Delta\nu_1$	0.73	−0.0017994

TABLE F4. PARAMETERS IN EQUATION A2
TO CALCULATE GAUSS FRACTION VALUES OF $MgCl_2$ BRINE
IN THE PRESENCE OF ICE AND VAPOR BUBBLE

	b_0	b_1	b_2	b_3
$\Delta\nu_1$	0.0	1.0	28.1524	36.7894
$\Delta\nu_2$	1.0	−1.0	378.424	66.4697
$\Delta\nu_3$	0.0	1.0	122.824	10.4693

APPENDIX G. $MgCl_2$ HYDRATE

TABLE G1. PARAMETERS IN EQUATION A1
TO CALCULATE PEAK VALUES OF $MgCl_2 \cdot 12H_2O$

	a_0	a_1	a_2
$\Delta\nu_1$	3519.4	−0.023424	−0.00010709
$\Delta\nu_2$	3464.2	0.011001	–
$\Delta\nu_3$	3402.7	0.0026945	0.00016458
$\Delta\nu_4$	3186.2	0.15331	–
$\Delta\nu_5$	3322.1	0.08361	−0.00078418
$\Delta\nu_6$	3433.6	0.033242	0.00012063
$\Delta\nu_7$	3484.4	−0.021596	–
$\Delta\nu_8$	3389.7	−0.064718	0.0011862

TABLE G2. PARAMETERS IN EQUATION A1
TO CALCULATE HALF-WIDTH VALUES OF $MgCl_2 \cdot 12H_2O$

	a_0	a_1	a_2
$\Delta\nu_1$	8.9767	0.041667	0.00027917
$\Delta\nu_2$	10.993	0.022382	0.00016458
$\Delta\nu_3$	22.073	0.079256	0.00019521
$\Delta\nu_4$	41.306	0.17022	–
$\Delta\nu_5$	23.243	−0.06908	0.0018587
$\Delta\nu_6$	36.302	−0.037997	–
$\Delta\nu_7$	11.972	–	–
$\Delta\nu_8$	283.89	−0.25826	–

TABLE G3. PARAMETERS IN EQUATION A2
TO CALCULATE GAUSS FRACTION VALUES OF $MgCl_2 \cdot 12H_2O$

	b_0	b_1	b_2	b_3
$\Delta\nu_1$	0.0	–	–	–
$\Delta\nu_2$	1.0	–	–	–
$\Delta\nu_3$	0.0	1.0	150.699	33.3631
$\Delta\nu_4$	1.0	–	–	–
$\Delta\nu_5$	1.0	–	–	–
$\Delta\nu_6$	1.0	–	–	–
$\Delta\nu_7$	1.0	–	–	–
$\Delta\nu_8$	1.0	–	–	–

TABLE G4. PARAMETERS IN EQUATION A1 TO CALCULATE AMPLITUDE RATIOS FOR THREE DIFFERENTLY ORIENTED CRYSTALS OF $MgCl_2 \cdot 12H_2O$

	$\Delta\nu_2/\Delta\nu_1$	$\Delta\nu_3/\Delta\nu_1$	$\Delta\nu_4/\Delta\nu_1$	$\Delta\nu_5/\Delta\nu_1$	$\Delta\nu_6/\Delta\nu_1$	$\Delta\nu_7/\Delta\nu_1$	$\Delta\nu_8/\Delta\nu_1$
				orientation 1			
a_0	0.171	0.0407	0.034	–0.0123	0.124	0.1253	–0.0933
a_1	0.00273	0.00387	0.0022	0.000967	0.0012	0.000933	0.00367
				orientation 2			
a_0	0.192	0.0767	0.0773	–0.0123	0.0693	0.0473	–0.1073
a_1	0.0016	0.00267	0.00153	0.000967	0.00113	0.000533	0.00347
				orientation 3			
a_0	0.0893	0.1353	0.1	–0.00567	0.0973	–0.0067	–0.056
a_1	0.00113	0.00193	0.001	0.000633	0.00053	0.000333	0.0022

APPENDIX H. $H_2O - MgCl_2$ – GLASS

TABLE H1. PARAMETERS IN EQUATION A1 TO CALCULATE PEAK VALUES OF $H_2O - MgCl_2$ – GLASS

	a_0	a_1
$\Delta\nu_1$	3444.5	–
$\Delta\nu_2$	3350.0	–
$\Delta\nu_3$	3107.3	0.15235
$\Delta\nu_4$	3177.5	–
$\Delta\nu_5$	3514.5	–

TABLE H2. PARAMETERS IN EQUATION A1 TO CALCULATE HALF-WIDTH VALUES OF $H_2O - MgCl_2$ – GLASS

	a_0	a_1
$\Delta\nu_1$	85.5	0.1938
$\Delta\nu_2$	289.3	–0.082005
$\Delta\nu_3$	80.055	–0.0216
$\Delta\nu_4$	137.32	0.21035
$\Delta\nu_5$	33.491	0.11792

TABLE H3. PARAMETERS IN EQUATION A1 TO CALCULATE AMPLITUDE RATIOS OF $H_2O - MgCl_2$ – GLASS

	a_0	a_1
$\Delta\nu_2/\Delta\nu_1$	0.48673	0.0005995
$\Delta\nu_3/\Delta\nu_1$	0.38297	–0.0016793
$\Delta\nu_4/\Delta\nu_1$	0.62178	–0.001158
$\Delta\nu_5/\Delta\nu_1$	0.3859	0.0011987

TABLE H4. PARAMETERS IN EQUATION A2 TO CALCULATE GAUSS FRACTION VALUES OF $H_2O - MgCl_2$ – GLASS

	b_0	b_1	b_2	b_3
$\Delta\nu_1$	1.0	–	–	–
$\Delta\nu_2$	1.0	–	–	–
$\Delta\nu_3$	1.0	–1.0	147.201	8.62919
$\Delta\nu_4$	1.0	–	–	–
$\Delta\nu_5$	0.0	–	–	–